A Wave Energy Converter for ODAS Buoys (WECO)

by

David Fiander
BEng, University of Victoria, 2008
Dipl Tech, Camosun College, 2003

A Thesis Submitted in Partial Fulfillment
of the Requirements for the Degree of

MASTER OF APPLIED SCIENCE

in the Department of Mechanical Engineering

Supervisory Committee

A Wave Energy Converter for ODAS Buoys (WECO)

by

David Fiander
BEng, University of Victoria, 2008
Dipl Tech, Camosun College, 2003

Supervisory Committee

Dr. Peter Wild, Department of Mechanical Engineering
Supervisor

Dr. Bradley Buckham, Department of Mechanical Engineering
Departmental Member

Abstract

Supervisory Committee

Dr. Peter Wild, Department of Mechanical Engineering

Supervisor

Dr. Brad Buckham, Department of Mechanical Engineering

Departmental Member

Ocean Data Acquisition System (ODAS) buoys are deployed in many seas around the world, a subset of these are wave monitoring buoys. Most are powered by solar panels. Many of these buoys are subjected to movement from waves, and could benefit from a wave energy converter specifically designed for ODAS buoys (WECO). A particular buoy that could benefit from this technology is the TriAXYS wave buoy [1]. This thesis discusses the development of a self-contained WECO that would replace one of the buoys four on board batteries, and harvest energy from the buoy motion to charge the remaining three batteries. A major constraint on the WECO is that it can't affect buoy motion and jeopardize wave data that is derived from the motion.

Rather than follow a traditional approach to simulating the motion of the buoy / WECO system, using hydrodynamic modelling and theoretical wave profiles, existing motion data from a buoy installation was analyzed to find the loads that were applied to the buoy to cause the motion. The complete set of mass properties of the TriAXYS buoy were derived from the 3D model provided by AXYS Technologies. These mass properties were compared to the linear and rotational accelerations to find the loads that were applied at the buoy center of gravity (CG) to cause the recorded motion.

An installation off the coast of Ucluelet, BC was selected for this investigation because it is subjected to open ocean swells, and data from the winter months of November to March of 2014 to 2016 is available. Winter data was used since there is more wave action to power the WECO during the winter months, and there is sufficient solar irradiation to power the buoy in summer months. Accurate buoy motion data at a 4 Hz sampling rate was available from three rotational rate gyros and three linear accelerometers installed in the buoy. Each dataset of samples represented a 20 minute window that was recorded once every hour.

Five conceptual WECO designs were developed, each of which focused on the extraction of power from a different degree of freedom (DOF) of buoy motion (surge, sway, heave, roll, and

pitch). Three designs used a sliding (linear) oscillating mass, and one was aligned with each of the surge, sway, and heave axis of the buoy. Two designs used a rotating oscillating mass, and the axis of rotation of each device was aligned with either the roll or pitch axis of the buoy.

All proposed WECO configurations were modeled as articulated mass, spring, and damper systems in MATLAB using the Lagrange method. Each WECO/buoy assembly formed an articulated body. Mass properties for each configuration were derived from the 3D models. The equations of motion for the original buoy no longer applied, but the environmental forces applied to the hull would still be valid as long as the WECO didn't alter motion significantly.

The power take off (PTO) was modeled following standard convention as a viscous dashpot. The damping effect of the dashpot was included in the models using Rayleigh's dissipation function that estimated the energy dissipated by the PTO.

A subset of load datasets was selected for evaluating the maximum power potential of each WECO. Each WECO was tuned to each dataset of loads using the spring rate, and the damping coefficient was optimized to find the maximum power while avoiding end stop collisions. A second subset of data was selected to evaluate the average power that would be generated throughout the winter months for the two most promising designs. This evaluation was performed for static spring and damping coefficients, and the coefficients that resulted in the highest power output were discovered.

The motion of the WECO oscillating mass with respect to the buoy was used in conjunction with the damping ratio to form an estimate of the ideal (i.e. with no mechanical or electrical losses) power generation potential of each WECO configuration during the winter months. The two leading WECO designs both had sliding (linear) oscillating masses, one was aligned with the surge axis and produced theoretical average of just over 0.5 W, the other was aligned with the heave axis and produced theoretical average of just under 0.5 W.

Table of Contents

List of Tables

List of Figures

Acknowledgments

To my supervisors, Dr Buckham and Dr Wild, thank you for your guidance and mentorship. To my wife, children, and family, thank you for your patience and support.

Nomenclature

WEC	≡	Wave energy converter
Buoy WEC	≡	A subset of WECs designed to provide operational power to the electronic systems contained in a floating buoy
WECO	≡	WEC for ODAS buoys. The specific buoy WEC system being considered for installation in, and to harvest power from the motion of, the TriAXYS buoy. This mechanism is internal to the buoy and is excited by buoy motion. It consists of an elastically supported reaction mass coupled to a power-take-off
PTO	≡	Power take off
CoM	≡	Center of mass
MoI	≡	Mass moment of inertia (second moment of mass about an axis)
Point *C*	≡	CoM of the buoy and WEC assembly, when the WECO oscillating mass displacement is zero (also the origin of the buoy frame of reference)
Point *G*	≡	CoM of the WECO mass
Point *B*	≡	CoM of the buoy without WECO (with the appropriate battery removed and the 4 kg block added)
Point *A*	≡	For linear WECOs, this is the location of the CoM of the WECO oscillating mass at rest For rotating WECOs, this is the location of the center of rotation of the WECO oscillating mass

α ≡ For linear WECOs, the linear displacement of the oscillating mass from rest, with respect to the buoy reference frame.

β ≡ For rotating WECOs, the angular displacement of the oscillating mass from rest about point A, with respect to the buoy reference frame.

$q_1 = u$ ≡ Linear velocity of point *C* in the surge direction, X

$q_2 = v$ ≡ Linear velocity of point *C* in the sway direction, Y

$q_3 = w$ ≡ Linear velocity of point *C* in the heave direction, Z

$q_4 = p$ ≡ Rotational velocity of the buoy about the roll axis, X

$q_5 = q$ ≡ Rotational velocity of the buoy about the pitch axis, Y

$q_6 = r$ ≡ Rotational velocity of the buoy about the yaw axis, Z

$q_7 = \dot{\alpha}$ ≡ For linear WECOs, the linear velocity of the WECO CoM, point *G* with respect to the buoy reference frame.

$q_7 = \dot{\beta}$ ≡ For rotating WECOs, the angular velocity of the WECO oscillating mass with respect to the buoy reference frame.

$\bar{\omega}_{Buoy}$ ≡ Rotational velocity of the buoy

$\bar{\mathrm{f}}_{\mathrm{PTO}}$ ≡ Unit vector in the direction of:

- motion for linear WECOs

- the axis of rotation for rotating WECOs

$\bar{\mathrm{n}}_{\mathrm{PTO}}$ ≡ Unit vector in the direction of the rotating WECO arm (rotating WECOs only)

$\bar{v}_C$ ≡ Absolute velocity of point *C*

$\bar{v}_B$	≡	Absolute velocity of point *B*
$\bar{v}_G$	≡	Absolute velocity of point *G*
$\bar{v}_{B/C}$	≡	Velocity of point *B* with respect to point *C*
$\bar{v}_{A/C}$	≡	Velocity of point *A* with respect to point *C*
$\bar{v}_{G/A}$	=	$\dot{\alpha} \cdot \bar{u}_{PTO}$ (for linear WECOs)
	≡	Velocity of point *G* with respect to point *A*
$\bar{\omega}_{G/B}$	=	$\dot{\beta} \cdot \bar{u}_{PTO}$
	≡	Rotational velocity of the WECO mass with respect to the buoy
$\bar{r}_{A/C}$	≡	Displacement from point *C* to point *A*
$\bar{r}_{G/A}$	≡	Displacement from point *A* to point *G*
$\bar{r}_{B/C}$	≡	Displacement from point *C* to point *B*
L	≡	Length of rotating WECO arm, the distance from point *A* to point *G* $\left(L = \left\|\bar{r}_{G/A}\right\|\right)$ for rotating WECOs
$\underline{I}_{Buoy}$	≡	Inertia tensor of the buoy, about its CoM without a WECO installed (and with the appropriate battery removed)
m_{Buoy}	≡	Mass of the buoy without WECO (and with one battery removed)
m_{WECO}	≡	Mass of the WECO
$\underline{I}_{WECO}$	≡	Inertia tensor of the WECO mass, taken about its CoM
k_{Spring}	≡	Spring rate [N/m for linear WECWECO's, N.m/radian for rotating WECOs]

c_{PTO}	≡	Damping coefficient representing the power take off system [N.s/m for linear WECOs, N.m.s/radian for rotating WECOs]
$c_{Critical}$	≡	The critical damping coefficient of the PTO
k	≡	WEC/WECO spring rate
ζ	≡	The damping ratio of the PTO
Hs	≡	Significant wave height
Ds	≡	Significant buoy displacement. Similar to Hs but related to buoy motion in one DOF rather than ocean surface heave displacement
Te	≡	Energy period associated with a significant wave height
m_n	≡	*n*th spectral moment of either ocean surface displacement or TriAXYS buoy displacement

Dedication

For my Mom

Chapter 1
Introduction

1.1 Background

A small wave energy converter (WEC) specifically designed for installation in a marine ocean data acquisition system (ODAS) buoy has not been previously developed. ODAS buoys consist of any range of sensors, coupled to an electronic data acquisition and control system, usually with onboard telemetry to transmit the collected data to shore. The power system of ODAS buoys is usually a battery bank that is charged by solar panels. Some existing ODAS buoys would benefit greatly from a robust device that would generate power from the wave motion they are constantly subjected to. Wave induced motion is a natural complement to the predominant renewable energy option for ODAS buoys: solar irradiation. During the winter months when solar irradiation is insufficient to maintain charge in the buoys batteries, wave energy is often at its peak. Poorly lit regions, extreme latitudes or deep fjords as examples, would be the primary target areas for deployment, however any offshore location could benefit from this additional energy source. Developing such a WEC for small widely used ODAS buoys (WECO) is the primary focus of this thesis.

An ODAS buoy that is well suited to this technology is the TriAXYS Wave Buoy [1]. The TriAXYS is a wave profiling buoy, when deployed it records buoy motion data that is later translated into wave profiles using a proprietary algorithm based on Fourier decomposition of the motion signals. Buoy motion data is recorded by 3 linear accelerometers, and three rotational rate gyros. The TriAXYS buoy can operate through extended deployment and long maintenance intervals, but a common maintenance requirement is to replace failing batteries. Throughout the winter months, the onboard solar panels often do not collect sufficient energy to meet the operational drain on the batteries. This results in a nearly complete drain of battery charge each winter, and after a few winters the batteries are no longer able to maintain the required voltage and must be replaced. It is for these winter months that a wave power converter would be most active and could maintain the charge of the batteries, thus increasing the length of maintenance intervals of the buoy. A further benefit of the WECO technology is that it could allow the

TriAXYS buoy to maintain higher sampling rates through the winter, thus increasing data quality; currently, sampling rates are decreased to conserve energy as the solar irradiation wains in the winter. These benefits would likely transfer to other ODAS buoys as well.

ODAS buoys like the TriAXYS are designed to withstand the harshest environments in the open ocean; they are well sealed against water ingress. Incorporation of a WECO must not jeopardize the impermeability of the buoy, therefore the device must fit within the buoy hull and be in the same air chamber as the power system. Onboard real estate on ODAS buoys is scarce, so finding available space for an additional mechanism in existing buoys is unlikely. ODAS buoys must currently be capable of storing enough power to get through long periods without solar irradiation. Installation of a WECO would reduce the energy storage requirement such that the storage would be required to get through periods without both solar irradiation and wave action. Thus, the space for the WECO could be acquired by removing a battery.

The WECO would be a standalone device and would replace one of the buoys' four batteries. Energy from the WECO would be delivered to the remaining three batteries. As an added benefit for future applications of this technology, the battery size is common among other buoys and so the same device could possibly be deployed in other ODAS buoys with minimal design changes.

1.2 Existing Technology

A WEC specifically designed to provide operational power to the electronic system contained in a floating buoy is not a new idea, research in the area dates back to the 1970s [2]. However, no research on a system purposely designed to fit inside existing ODAS buoys has been published, and there are no technologies that are applicable to a fully contained device that could be adapted for this application. There are no WEC designs known to be currently under evaluation that utilize one floating body with a contained oscillating mass.

When considering the TriAXYS buoy hull as a WEC, it would be classified as a point absorber due to its hull shape and size. Point absorbers are defined as devices with small extension compared to the wavelength of ocean waves [3]. These can be further broken into three groups; heaving, surging/swaying, and pitching/rolling/rocking devices. Heaving point absorbers focus on generating power from the vertical or heave motion of the WEC. Surging/swaying point absorbers generate power mostly from the horizontal, surge or sway, motion of the WEC.

Finally, rocking point absorbers are designed to collect power from the pitching or rolling motion of the WEC. The TriAXYS moves in all of these degrees of freedom (DOF), and so could be considered as any of those three point absorber subclasses depending on the wave power absorbing system that was installed.

WECs are not the only devices capable of converting physical motion into usable energy. In other distinct technology applications, teams are developing energy harvesting techniques. An example is energy harvesters in portable electronic systems such as cell phones and watches. Apart from the few devices for powering wrist watches, all of the explored systems are only suitable for very small scale use. This is due to the use of expensive materials such as piezoelectrics, and reliance on extremely tight manufacturing tolerances to take advantage of electromagnetic phenomena [4]. These two factors remove many of the technologies discovered from consideration for the device in question.

An overview of the technology used in self powered watches will be presented and their possible applications outlined. Four rocking/surging WECs are outlined as they are the only devices which have fully contained generation devices. No heaving point absorber technologies were found which have fully contained generation systems. Also, two selections from the patent literature will be presented that could possibly be adapted for application to the TriAXYS buoy platform.

1.2.1 SEAREV

The SEAREV device was first introduced by Barbarit et al. in 2003 [5] and was the subject of two patent applications. The first was in 2005 [6] and the second in 2009 [7]. It uses a free spinning pendulum, not spring loaded and with no end stops, to capture the induced motion from the waves. The proposed device uses a hydraulic power take off system (PTO) utilizing linear cylinders, an accumulator, and hydraulic motor to turn an electric generator, see Figure 1.1. There have been thorough investigations into the shape of the floating body [8], the effect of latching control [9], and declutching control of the hydraulic PTO [10]. This device has shown promising results for grid applications due to its robustness, simplicity, low environmental impact, and ease of scalability through array deployment, among others [11].

The floating portion of the hull is oriented lengthwise into the approaching waves, causing the buoy to pitch with the waves. The oscillating mass is oriented to extract power from the pitching motion, and the shape of the hull was optimized to amplify motion in that DOF. A pendulum style oscillating mass was originally designed for the system as shown in the figure, however a large inertial cylinder was envisioned for the next iteration of the design, but further work if completed was not published. In 2015, the estimation of the cost per unit of power was deemed too high for the SEAREV to justify further testing [12].

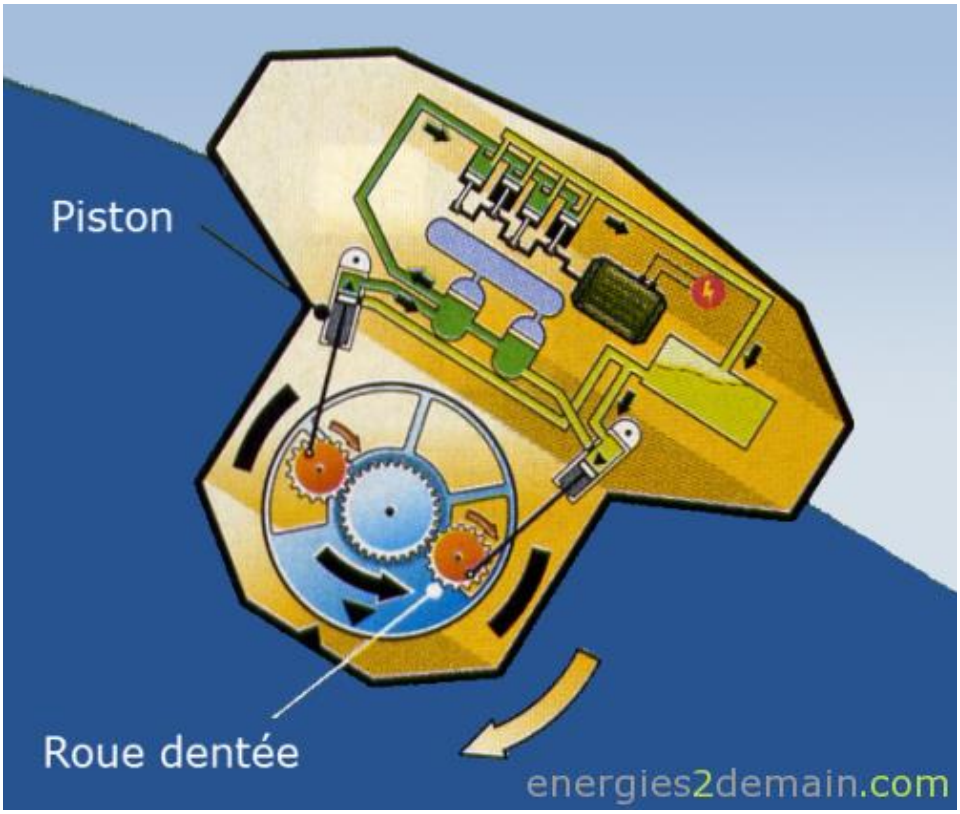

Figure 1.1 – The SEAREV WEC [13]

Although this device has application to the device in question, a direct use of the device is not possible. The main reason is that extensive research was performed to develop the appropriate shape of the hull. It is long and narrow so that it pitches aggressively thus inducing rotation on the pendulum. Early analysis of the TriAXYS buoy indicates there is insufficient pitching motion to extract the required power using this type of WEC.

Another reason the device is not directly applicable is due to the hydraulic PTO. The hydraulic PTO would not be desirable for the device in questions due to the increased pressure loss due to

small tubing that would need to be implemented as the concept is scaled down to fit within the TriAXYS buoy's battery enclosure, and the use of valuable real estate for these tubes and associated components, i.e. pump, accumulator, motor.

1.2.2 PS Frog Mk 5

The PS Frog Mk 5 WEC is similar to the SEAREV. However instead of aligning the long axis of the hull with the wave direction, it aligns at 90 degrees to the wave direction and makes use of a submerged ballast and paddle to induce the pitching motion that is transferred to the oscillating mass. It uses a sliding reaction mass coupled with a PTO that includes an advanced control system to tune the oscillations to the waves acting on the hull, see Figure 1.2. The latest publication on this WEC [14] was published in 2006, it is therefore likely that the device was found to be unviable since no further work has been reported for over a decade.

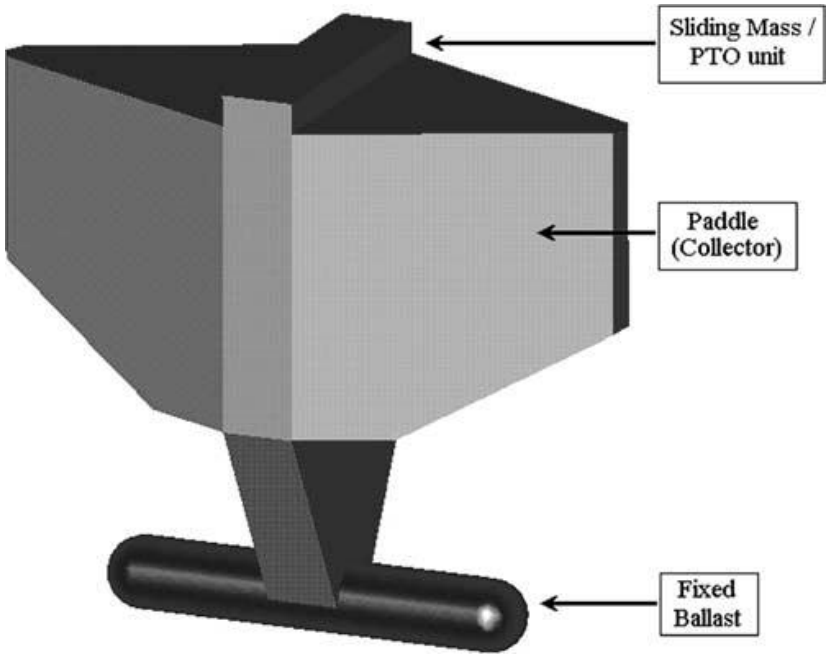

Figure 1.2 – PS Frog Mk 5 WEC [14]

1.2.3 Gemmell and Muetze's Rocking WEC

Another point absorber WEC exploiting an internal reaction mass is the rocking WEC developed by Gemmel and Muetze [15]. The device is unnamed but is shown in Figure 1.3. It

was similar to the SEAREV and operated on the same principles as the SEAREV design, but it proposes the use of a curved linear generator as the PTO. The lone paper written on the device [15] heavily referenced the development of the SEAREV and PS Frog devices.

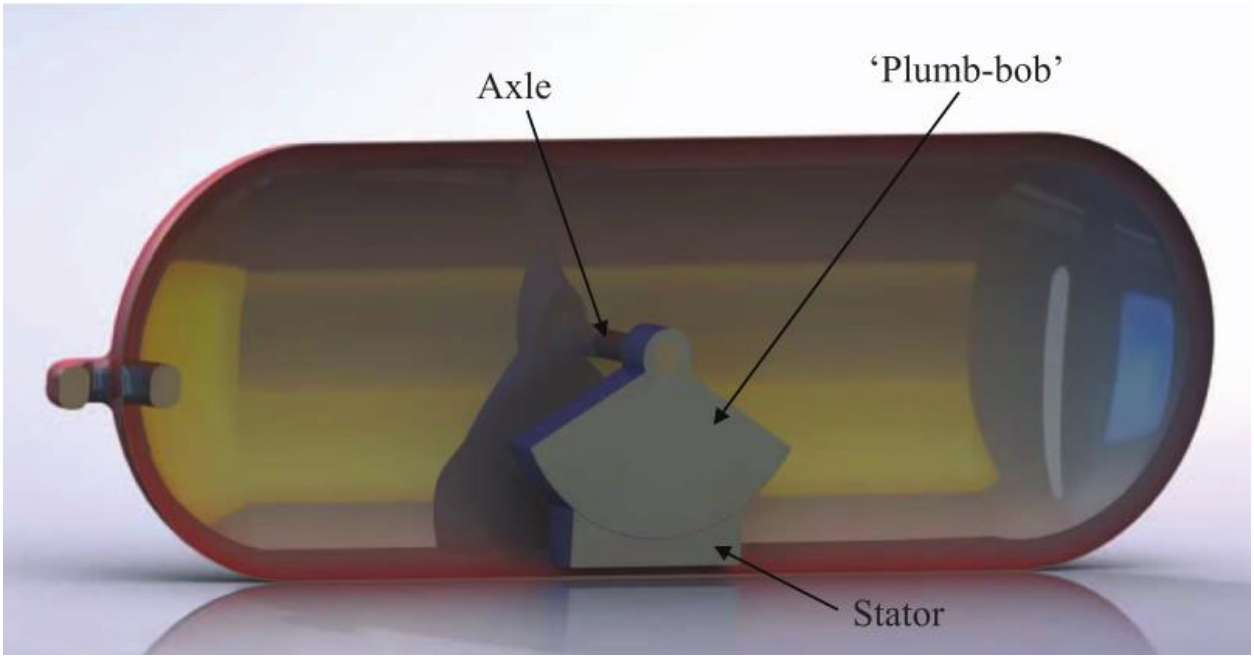

Figure 1.3 - Gemmell and Muetze's Rocking WEC [15]

1.2.4 Inertial Pendulum WEC

Some analysis has been performed on the potential of using an inertial pendulum system to power autonomous underwater vehicles [16] [17], see Figure 1.4. That research established ideal theoretical capture width ratios for a submerged spherical buoy with an inertial pendulum similar to that in the SEAREV. Further articles on this device were not found.

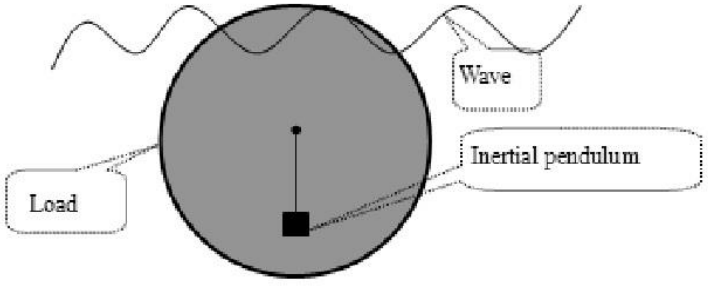

Figure 1.4 – Submerged Inertial Pendulum WEC [16]

1.2.1 The User Powered Watch

User powered watches harvest power from the motion of the user to either wind a coil spring, or turn an electric generator which charges a battery. It is very old technology. The first self-winding watch was presented in Switzerland in 1770 [18]. While slight differentiations occur from one design to another, most work on the same design principle. The technology uses a free spinning pendulum, connected through a gear train or pawl lever mechanism which rectifies the rotation, to either the winding system mechanism of a mechanical watch, or a small generator for powering an electronic watch. This design is remarkably similar to the WECs described in Sections 1.2.1, 1.2.3, and 1.2.4, the major difference being that watches utilize a pawl lever and gear train to rectify the rotational output of the pendulum. A pawl lever mechanism is shown in Figure 1.5.

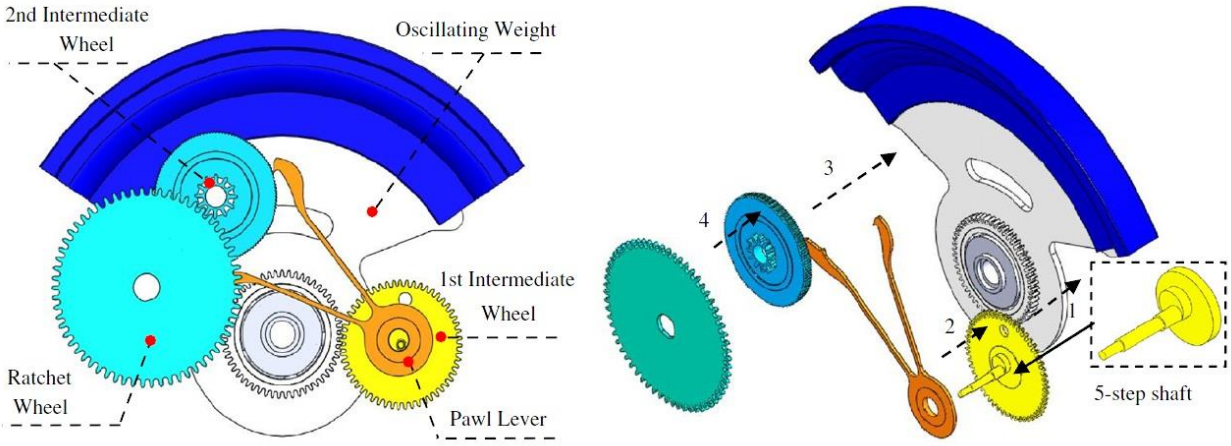

Figure 1.5 – Pawl lever mechanism [19]

The efficiency of the drive configuration shown in Figure 1.5 was completed by L. Xie et al. [20]. They found that the device operated at an efficiency of 46%. Most of the energy loss is due to the four sets of gears used to convert the oscillating motion of the weight into a single direction rotation of the winding spring, estimated at 65% efficiency. Therefore, removing the gear sets for directional conversion would leave 70% efficiency for the rest of the power converter.

Another interesting device designed for powering watches uses a rotating weight as a rotor for an electric generator [21]. This device is similar to other direct drive power converters such as

[15]. There are also many other patents involved with providing a solution for powering watches, but none were found that applied to the device in question.

1.2.2 Rocking Motion to Electrical Energy Converter

In 1988, a patent was given to R.E. Soloman for a device that converts a rocking motion to electric power [22]. The conversion process is based on fluid oscillating in a tube as the tube is rocks back and forth. The ends of the tube are connected through a turbine which generates electricity, as seen in Figure 1.6. Part 46 is a motor that imparted the rocking motion to the device for testing, and so is not part of the functioning device.

This is an interesting design and may be applicable in applications where other generator configurations would not be possible, because a flexible hose could be used and adapted to different operating environments. It is, however, expected that the use of fluid for the device in question would not make sense for risk of damaging the batteries or other buoy electronics, and due to the losses in fluid pressure with flow.

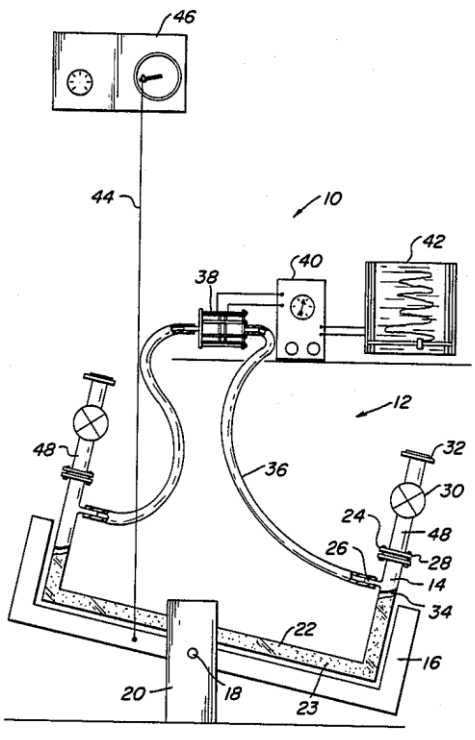

Figure 1.6 – A device which converts rocking motion into electrical power [22]

1.2.3 Gyroscope-Based Electricity Generator

In 2005, a patent was issued to A. Goldin for a WEC that uses gyroscopic inertia to convert wave energy [23]. The basic premise is that a spinning gyroscope resists rotation about any axis not parallel to its rotational axis. It therefore works like the mass of a free pendulum except that it is the gyroscope resisting motion of the pendulum instead of the force of gravity. Figure 1.7 shows a possible layout of the device. This technology could be useful for the device in question if it is found that weight is a constraining factor on power generation. The use of a gyroscope can effectively increase the rotational inertia of a pendulum without increasing the weight.

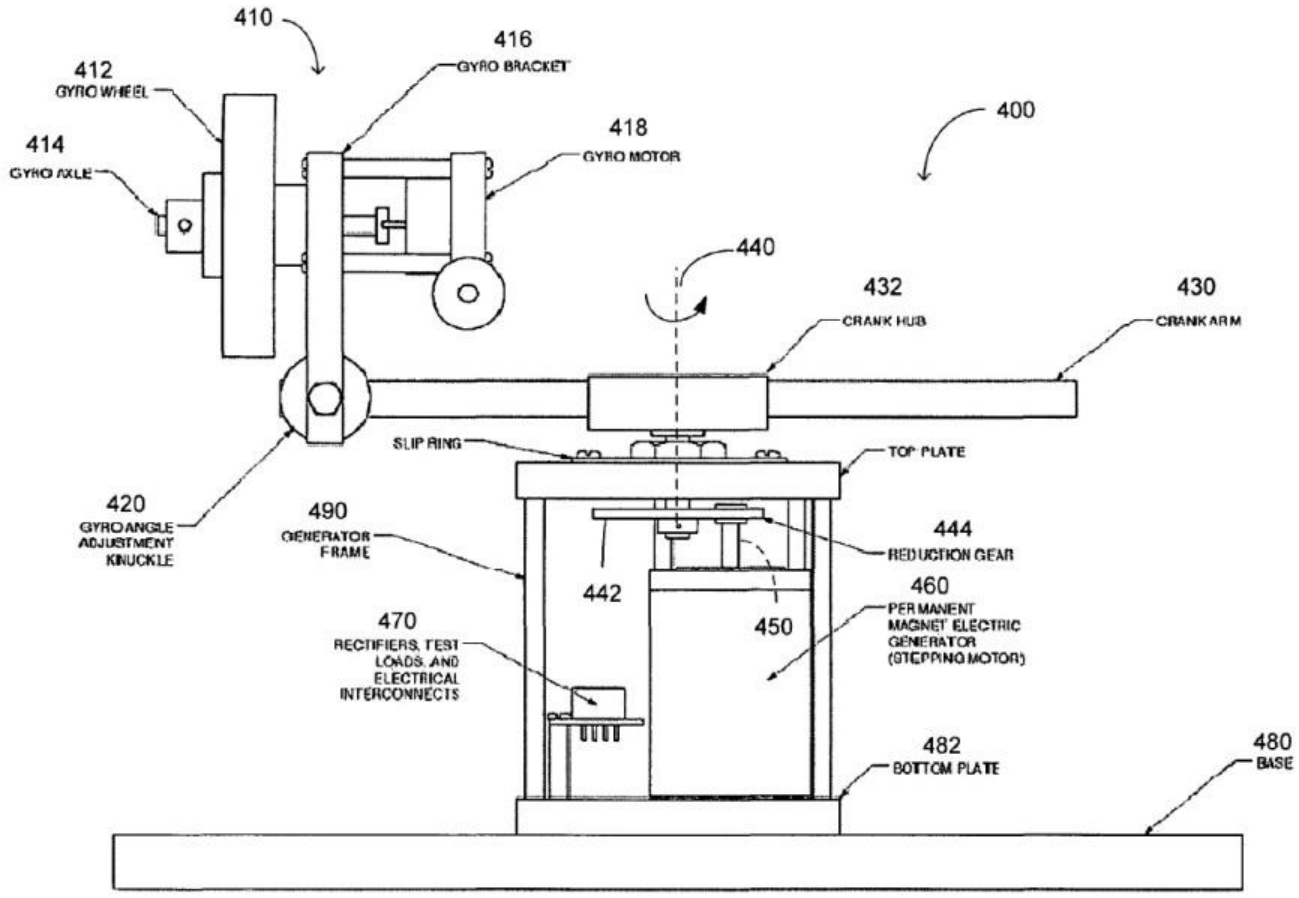

Figure 1.7 – Gyroscopic-Based electricity generator [23]

1.2.4 Direct Drive WECs

Energy harvesting technology utilizes a PTO that is separate from the oscillating mass, as can be seen in most of the examples above. One exception is what was proposed for Gemmell and

Muetze's WEC [15]. Direct drive electric generators for use in WECs have been developed that are capable of generating electricity at the relatively slow oscillating speeds found in WECs [24]. A linear direct drive system with a cross section as shown in Figure 1.8 has been verified experimentally [25], and methods of control and conditioning of the output have been studied in [26] and [27].

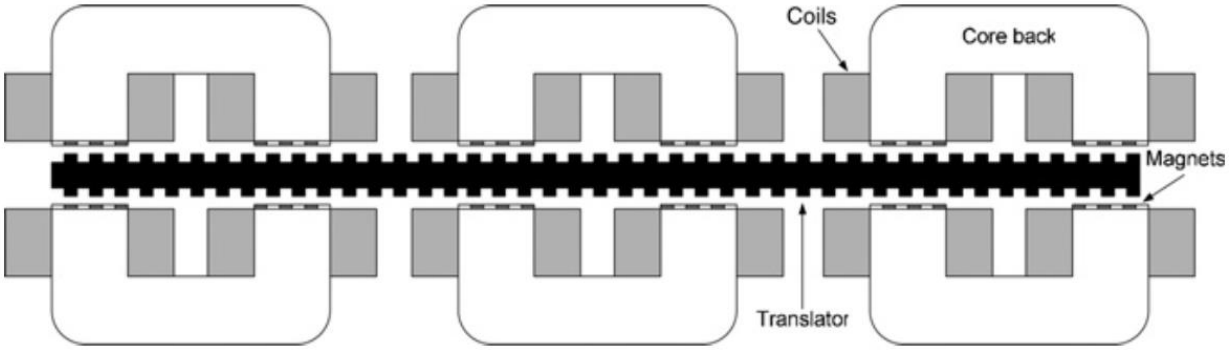

Figure 1.8 – Cross section of a direct drive linear generator [25]

1.2.5 Summary of Existing Tech

There is a plethora of proposed technologies for converting oscillatory motion into usable electricity, but there are a few components that are common among all forms. Each of the devices consist of an oscillating reaction mass and a PTO, sometimes these two parts are integrated in a direct drive system. Most energy harvesting devices also feature a spring attached to an oscillating mass, while other devices utilize a free spinning mass. The internal reaction mass and PTO has so far not to been found to be viable for large scale, grid connected, WECs such as in [12] and [14], however this does not rule out their application here. Table 1.1 shows a summary of the moving mass topology that was selected for each energy harvesting application reviewed above.

Table 1.1 - Summary of the topologies of the reviewed energy harvesting devices

Device	**Moving Mass Topology**
SEAREV [12]	Free Spinning Pendulum (A sliding linear mass was envisioned for the next iteration of the device)

PS Frog Mk 5 [14]	Sliding Linear Mass
Gemmell and Muetze's [15]	Vertical Pendulum with Spring
Inertial Pendulum [16]	Vertical Pendulum
User Powered Watch [19]	Free Spinning Pendulum
R.E. Soloman [22]	Fluid Oscillating in a Horizontal Tube
Gyroscope-Based [23]	Rotating Disc Resisting Motion of a Free Spinning Pendulum
Direct Drive [25]	Linear Oscillating Mass

A lot of work has been focused on analyzing how oscillatory motion of an oscillating mass installed on a floating platform could be used to generate electricity, however little attention has been paid to the effect of the oscillating mass on the motion of the floating platform. Based on current literature it is not obvious how well the TriAXYS buoy would drive any oscillator topology. A top priority of this work is to select the appropriate WECO topology for the TriAXYS buoy, with further design and development to include the PTO and other mechanical, electrical, and possibly controls strategies to be completed by others.

Evaluations of both linear and rotating masses are included in this work. Free spinning pendulums are not included for modeling reasons that will be explained below in Section 1.3. However, a free spinning pendulum mass that rotated about the surge axis was drawn in 3D. In order to meet the weight requirement in Section 1.4 and rotate 360 degrees without penetrating the battery envelope, it was shaped like a half donut and the distance from the axis of rotation to the center of mass (CoM) was very short (i.e. the pendulum length was very short). Due to this, it is expected that the oscillating systems that were modeled would outperform the free spinning pendulum that met the physical constraints.

1.3 WEC Modelling Techniques

The two more heavily researched devices out of those listed above, SEAREV and PS Frog Mk 5, were studied using conventional methods for evaluating floating point absorber WECs [14]

[8]. The hydrodynamic properties of the hulls were estimated based on characteristic hull shape variables, and dynamic equations were derived to represent the oscillating reaction mass and the associated PTO. Theoretical wave profiles, that were representative of the expected deployment sites for each device, were applied to these systems of equations. The hull shape and reaction mass/PTO variables were optimized along with other parameters, such as representative cost functions [28], to determine the device specifications most likely to provide the highest output power at the lowest cost [14] [8].

A departure from this approach is investigated in this thesis. Rather than developing a model that estimated the external loads applied to the buoy by application of characteristic simulated sea states to a hydrodynamic model of the TriAXYS hull and mooring, real world recorded buoy motions are used to estimate the loads that were required to move the buoy through its recorded motion. These loads include all loads that were applied to the buoy including wave, wind, and mooring loads. This was attempted for a number of reasons:

- Wave and mooring loads are difficult to estimate accurately, especially when the buoy hull is essentially a simple sphere. It was important to include the correct rotational buoy excitation in the model because that was seen as a DOF that could be tapped while having very little effect on the wave data.
- The TriAXYS hull was fixed and so hull optimization was not an option.
- Buoy motion data for the TriAXYS buoy is available from locations all over the world, any installation could be pre-screened using this approach to adjust operating variables of the WECO.
- Motion data from other buoys could be evaluated using the same approach to see if the WECO technology could be viable in other buoys.

One drawback of this approach was that devices that relied on the force of gravity to impart motion, such as free spinning and/or vertical pendulums, could not be evaluated. This was because the load data had to be centered, thus removing the gravitational loads, and because the output motions were postprocessed to remove noise and so actual device orientations were not available for computations during simulations. This drawback was accepted, see reasons at the end of Section 1.2.5.

1.4 Device Requirements

As was apparent from the review of energy harvesting technology, any self contained WEC or WECO must include an oscillating reaction mass housed inside a frame. A PTO is required to extract energy from the movement of the reaction mass with respect to the frame, and a spring is often installed to help tune the natural frequency of the system to the activating motion, thereby increasing the oscillating motion and the potential power. Since size and weight were critical to the design, a direct drive electric PTO was envisioned. Any alternatives PTO, such as hydraulic, pneumatic or gear train systems, would introduce more losses and utilize more space since they would still have to be coupled to an electric generator.

The WECO must meet the following constraints and requirements:

Table 1.2 - WECO requirements

Size:	The WECO must fit completely within the volume of one existing battery and have a similar mass, so that the buoy dynamics are not affected. - The specifications of one battery are: ▪ Size: 30.7 cm x 17.5 cmx 22.4 cm (12.1” x 6.9” x 8.8”) ▪ Mass = 30 kg (67 lbs)
Power Budget:	The buoy draws 72 Wh /day which equates to 3W continuous power from four batteries. Therefore, the WECO must provide at least ¼ of the continuous power, or 0.75W.
Cost:	Final build cost should be under $500.
Reliability:	Must have maintenance interval of greater than 5 years under expected sea states.
System Performance:	- No part of the system may pierce the buoy hull. - The ability of the buoy to measure accurate wave data, especially within frequency spectrum of reported data of 0.03 to 0.63 Hz, must not be affected.

One of the most important constraints on the WECO design was that it had to have a long maintenance interval. Minimizing the end stop contact was an important parameter for ensuring a robust design. End stop contact was also foreseen as being detrimental to the wave measurement capability of the buoy, since end stop contact would result in spikes in energy transfer from the oscillating mass to the buoy that could affect the instantaneous accelerometer and rate gyro measurements.

Minimizing the end stop contact meant that either a variable spring and / or damping ratio would be required, or else a single static spring rate and damping ratio pair must be selected that would limit the maximum oscillation amplitude of the WECO to the maximum allowable. Early results indicated that maximum oscillation amplitude and power generation potential were correlated, and so maximizing the oscillation amplitudes without going over became the goal of the tuning. A static spring rate and damping ratio pair would be far simpler to achieve during future design and construction than variable rates. A static spring rate and damping ratio was therefore required that would maximize power while satisfying the maximum oscillation amplitude requirement.

1.5 Objectives

The main objective of this thesis was to discover the physical design attributes of the most promising WECO configuration for a TriAXYS buoy including: the shape of the oscillating mass, direction of oscillation, spring rate (k) and damping coefficient (ζ), and the particular battery that should be replaced out of the four options.

The most promising WECO configuration would produce the highest average power throughout the winter months, and would meet the requirements outlined in Section 1.4. The measure of power is restricted to the theoretical power removed from the system by the PTO. The output of this work will guide future mechanical design of the system, including discovery of the operational efficiency of the selected PTO.

A secondary objective was to utilize available buoy motion data as the input to simulations rather than a traditional approach. Using measured real-world inputs could provide more accurate results over simulated waves applied to a hydrodynamic model, and could enable the evaluation

of other wave buoys and / or other locations where motion and buoy dynamics data was available.

1.6 Overview

This thesis is structured as follows.

Chapter 2 introduces the TriAXYS buoy, the constraints on the proposed WECO, and the WECO designs that were evaluated.

Chapter 3 describes the buoy environment, the loads and the available data. It also introduces a new approach to modeling the system using a series of real world combined loads in the place of a hydrodynamic model.

Chapter 4 delves into the derivation of the equations of motion, including the technique for modeling the PTO. The physical values of vector lengths and mass properties are tabulated.

Chapter 5 outlines how the models were validated to ensure the results of the simulations were accurate.

Chapter 6 lays out the analysis that was performed on all WECO configurations, and how the average output power through the winter months was calculated for the two most promising configurations.

Chapter 2
WECO Installation in the Buoy

2.1 TriAXYS Buoy

The TriAXYS buoy is a purpose-built wave profiling buoy. The buoy shell is watertight, and protects an electronic system from the harsh environments of the open ocean. Figure 2.1 shows an exploded view of the main components of the system [1].

Figure 2.1 – Exploded view of the TriAXYS buoy [1]

The mass of the buoy is 204 kg, and the spherical shape is approximately 1 m in diameter. It is well balanced and stable when floating (i.e. the CoM is below the center of buoyancy, and located on the central vertical axis passing through the geometric center of the buoy). The mooring is attached to a lug welded to the bottom center of the hull. Onboard telemetry is usually installed that allows for two-way data transmission via radio, satellite, or cellular, so that the buoy status and collected data can be transmitted, and new instructions can be received.

2.1 Physical Constraints

Two dynamically unique battery locations exist in the buoy, location 1 and location 2, these are viewed from above and labeled in Figure 2.2. The X (surge) and Y (sway) directions are also shown, it follows that the Z (heave) direction is vertical with positive motion downward. The battery locations opposite to these would have similar but reversed motions, and so were not dynamically unique and were not modelled (i.e. placing a mirrored version of the same WECO in a battery location opposite to either location 1 or 2 was assumed to have the same theoretical power generation potential as the original non-mirrored device).

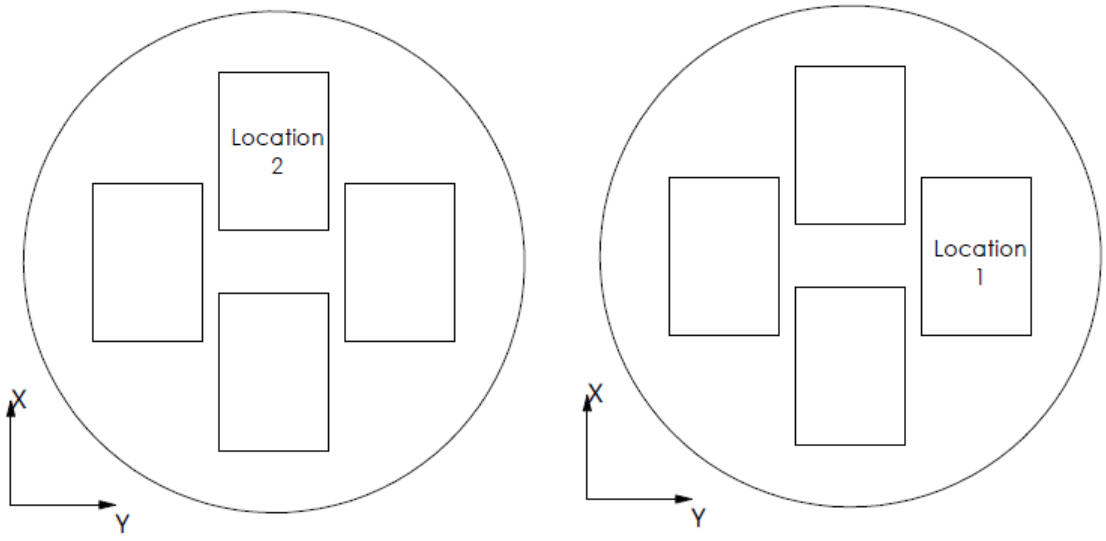

Figure 2.2 – Two possible WECO locations

Location 1 is in the positive Y direction from the buoy CoM, meaning that it is subjected to more excitation due to the rolling motion of the buoy than location 2. Location 2 is in the positive X direction from the buoy CoM, and it is therefore subjected to more excitation due to

the pitching motion of the buoy than location 1. These factors were considered when deciding on the orientation of the rotating WECO designs when placed in each location.

Each WECO was designed to fit within the physical space of a battery, and have the same total mass. This kept the dynamic properties of the buoy with the WECO installed similar to the original buoy with four batteries installed.

A common assumption was applied across all WECO designs, of the 30 kg battery that was removed, 4 kg was allotted to the PTO mass and other components of the WECO, and the WECO oscillating mass was set at 26 kg. This estimate was based on engineering judgement and may need to be revised during detailed mechanical design.

2.2 Proposed WECO Designs

Five WECO designs were developed to fit inside a rectangular battery envelope. Each proposed WECO design was 3D modelled so that the maximum oscillation amplitudes, between mechanical end stops, could be found. The PTO mass was drawn as a 4 kg cube, and the shape of each WECO oscillating mass was adjusted until an oscillating mass of close to 26 kg was in place and the maximum displacements were available for oscillation. The density of lead was used for the density of the WECO oscillating mass.

Each WECO design would be subjected to different motions depending on which battery location it was installed in, and so a unique model of the buoy with each WECO installed in each location was created. Both battery locations were oriented in the same direction with respect to the buoy frame (i.e. the long dimension of the battery is aligned with the surge axis), and since each WECO design was designed to fit within the rectangular envelope of a battery, the orientation of each WECO design with the buoy frame was the same in each location.

Each WECO design was analyzed for installation in each of the two battery locations, see Figure 2.2, resulting in 10 unique WECO configurations (note: a WECO configuration defines both the WECO design and the installation location on the buoy, either location 1 or 2.)

Two rotating WECO designs were considered, each envisioned to use a direct drive rotating electric PTO such as was proposed in [15]. One had a shorter pendulum length and rotated along an axis parallel to the long side of the battery volume (see Figure 2.3), the other had a longer pendulum length with a rotational axis parallel to the short side (see Figure 2.5). Rotating

WECOs were designed so that the initial spring deflection cancelled with the force of gravity so that the CoM of the oscillating mass at rest was level with the axis of rotation in the heave direction, as shown in the respective figures.

Three linear WECO design options were evaluated, these were envisioned to use a direct drive linear electric PTO, such as in [24] [25] [29] [27], no conversion to rotating motion was planned. Each design was created to focus on energy harvesting from one of the three linear degrees of freedom, each one with an oscillator shape designed to maximize the allowable oscillation amplitude along a single axis (either the surge, sway, or heave axis).

A fourth linear option was envisioned that would move in all three linear directions, but the complexity associated with such a device was considered too great to be viable. Such a device would require three separate linear PTOs, or a mechanical coupling of the three DOFs into one prior to power extraction. Creating a robust design of a single DOF WECO that would fit within the allotted space was a significant challenge, and due to the foreseen additional complexities with a three DOF WECO it was not pursued here.

2.2.1 Short Rotating WECO

The short rotating WECO is shown in Figure 2.3, along with the orientation of the local reference frame of the buoy. The axis of WECO rotation is parallel with the X axis of the buoy. The pendulum length L is relatively short, since it is oriented across the short dimension of the battery. The maximum oscillation amplitude in either direction is 21°, as shown on the drawing. The CoM of the WECO oscillating mass point *G*, along with the intersection of the axis of rotation and the plane of rotation of point *G*, referred to as point *A*.

The WECO oscillating mass was placed in the positive Y direction from the axis of rotation. This was done so that when installed in location 1 (see Figure 2.2) it would have the best chance of harvesting energy from the rolling motion of the buoy, as opposed to installing the WECO with the oscillating mass inboard of the axis of rotation and closer to the buoy CoM. When installed in location 2, it should not matter which side of the axis of rotation the oscillating mass was installed on. If this style of device was to be installed opposite to location 1, the device should be rotated 180° about the Z axis so that the oscillating mass is as far outboard from the buoy CoM as is possible.

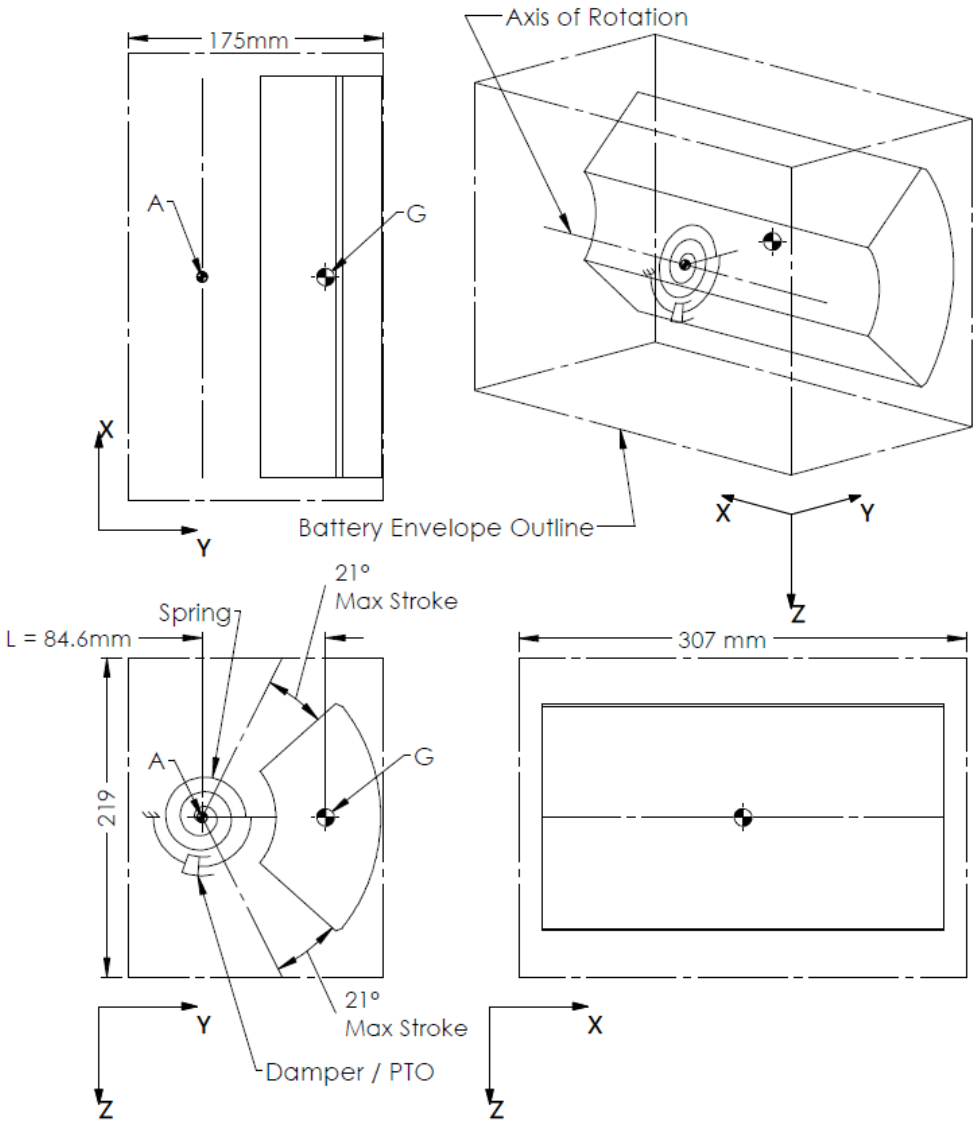

Figure 2.3 – Short rotating WECO positioned within the rectangular battery envelope, rotates about the X (roll) axis of the buoy

Figure 2.4 shows the buoy/WECO configuration with the short rotating WECO design installed in location 1 of the hull. Note that when this short rotating WECO design was moved to location 2, the orientation did not change as it still rotated about an axis parallel with the X axis of the buoy and point *G* was still located in the positive Y direction from point *A*. The Buoy hull has been made transparent to view the WECO. The stationary 4kg block representing the PTO can be seen at the center of rotation of the WECO, this place holder for the PTO and other equipment was included in the dynamic model of each configuration.

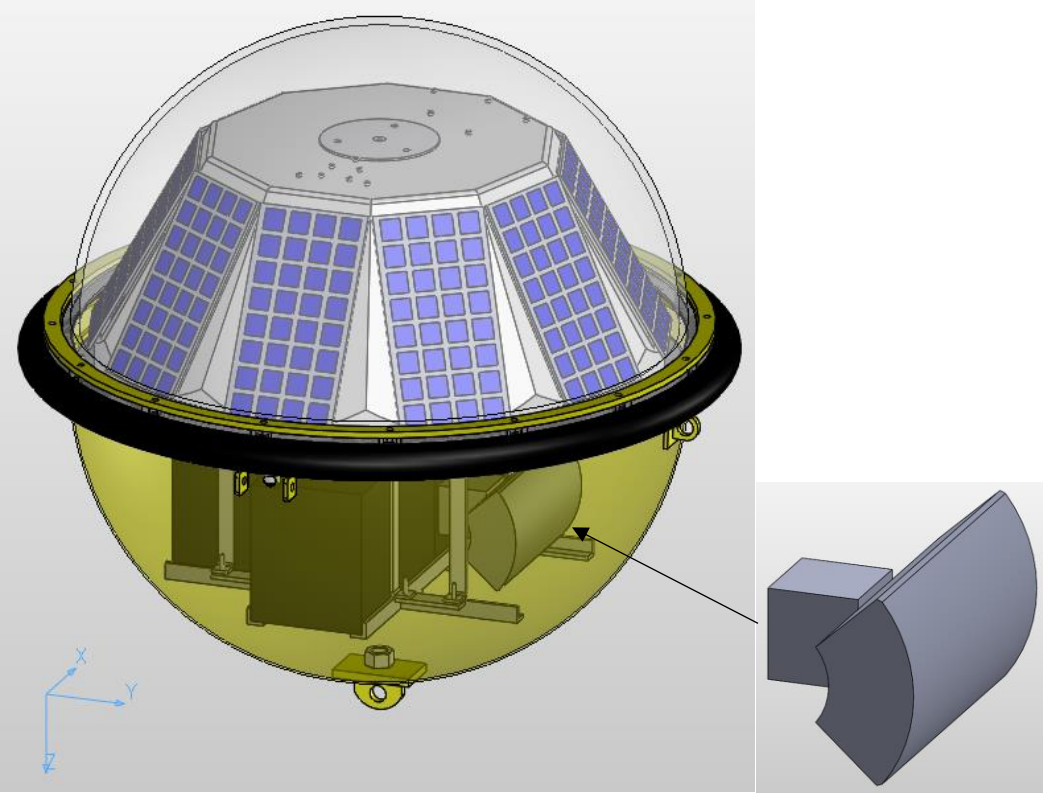

Figure 2.4 – Rendering of the short rotating WECO installed in location 1.

2.2.2 Long Rotating WECO

The long rotating WECO is shown in Figure 2.5. The pendulum length is relatively long, since it is oriented along the longest dimension of the battery. The maximum allowable oscillation amplitude is 9 degrees in either direction from rest.

The WECO oscillating mass was placed in the positive X direction from the axis of rotation. This was done so that when installed in location 2 (see Figure 2.2) it would have the best chance of harvesting energy from the pitching motion of the buoy. When installed in location 1, it would not matter which side of the axis of rotation the oscillating mass was installed on (positive or negative in the X direction).

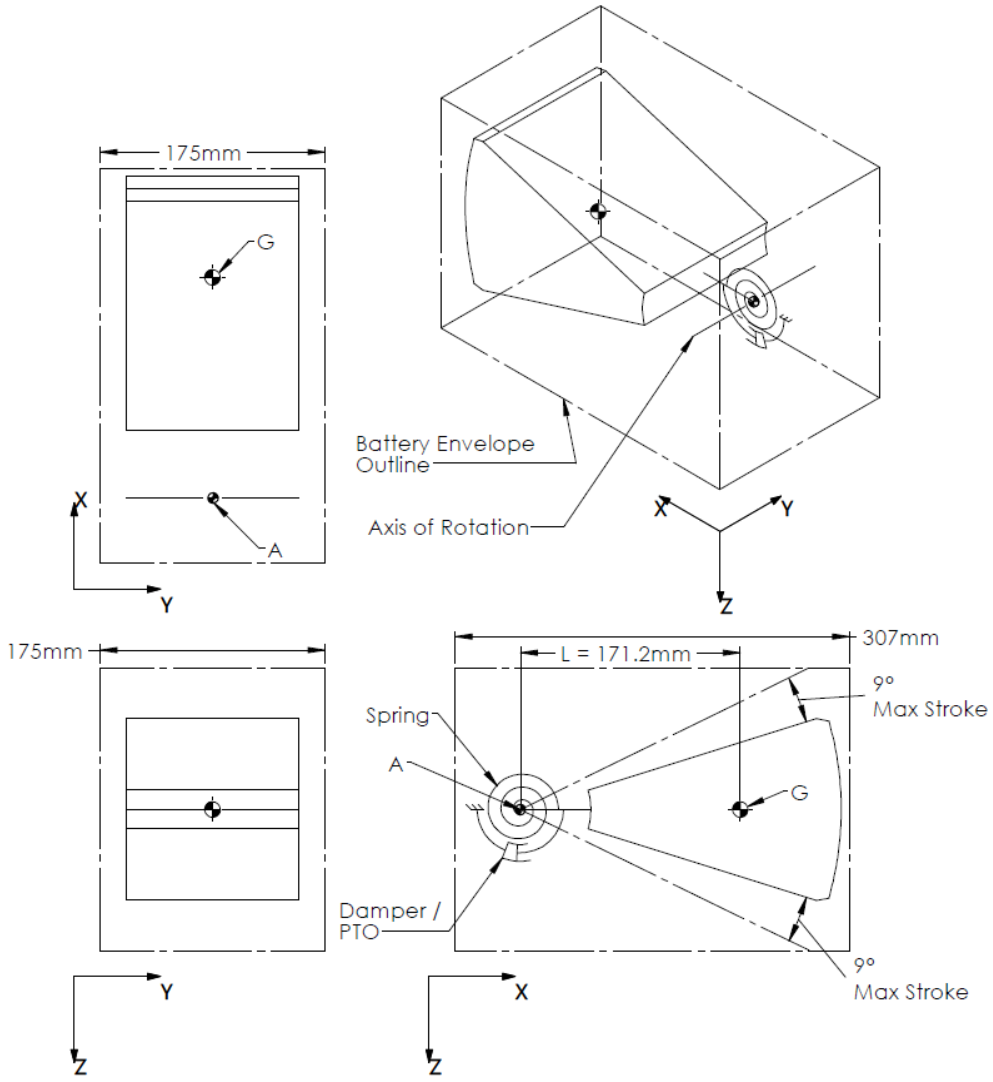

Figure 2.5 - Rotating long WECO, rotates about the Y (pitch) axis of the buoy

2.2.3 Linear X WECO

The linear X WECO is constrained to move only along the X axis of the buoy. The maximum amplitude of oscillation is 0.11m. A linear spring and PTO are shown, along with points *A* and *G*. For linear WECOs, point *A* is the location of the oscillating mass at rest, and is stationary with respect to the buoy frame. Point *G* is the CoM of the WECO oscillating mass and moves with respect to the buoy frame.

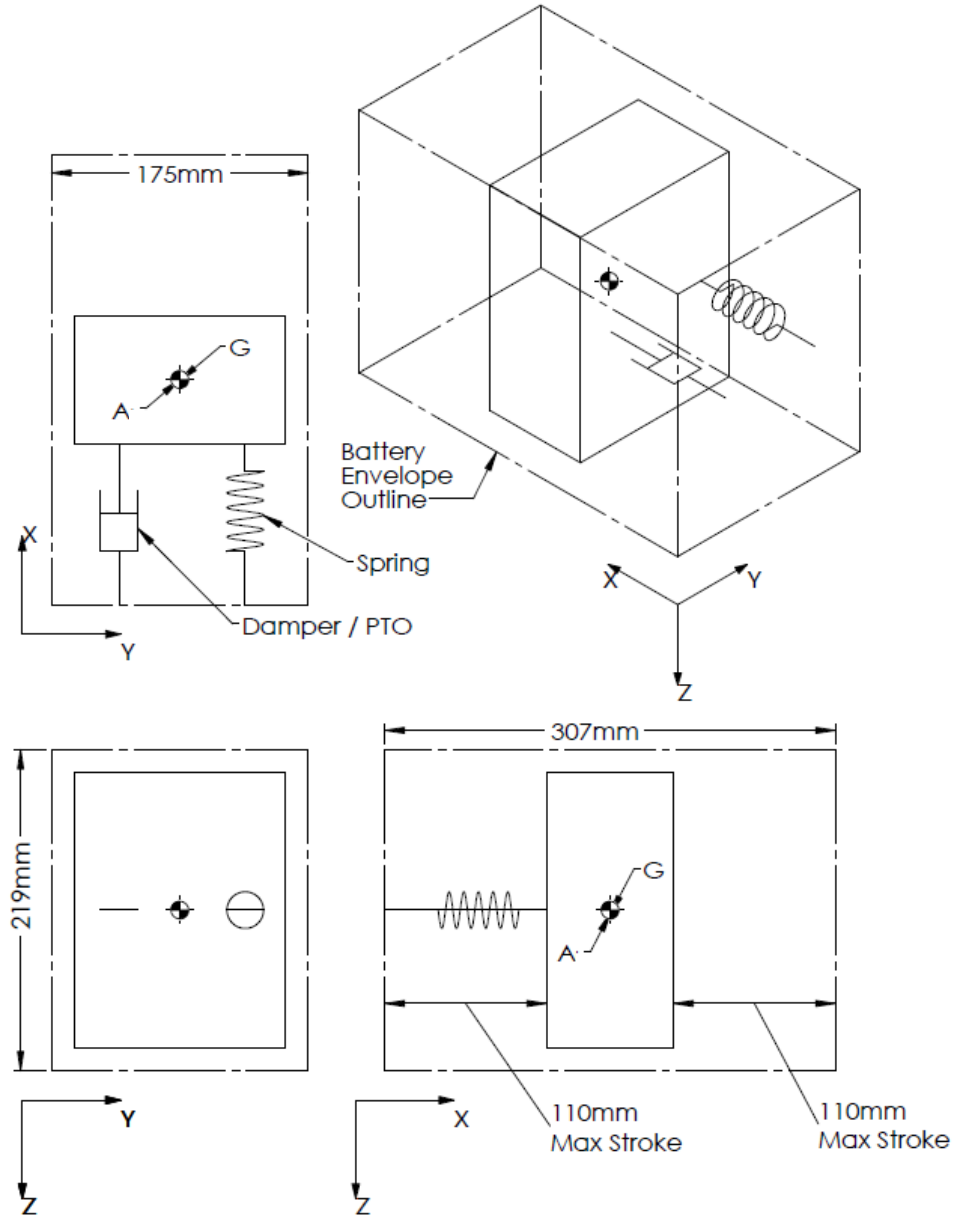

Figure 2.6 – Linear WECO with movement in surge (X) direction

2.2.1 Linear Y WECO

The linear Y WECO is constrained to move only along the Y axis of the buoy. The maximum amplitude of oscillation is 0.065m. A linear spring and PTO are shown, along with points *A* and *G*. Point *A* is the location of the oscillating mass at rest, and is stationary with respect to the buoy frame. Point *G* is the CoM of the WECO oscillating mass and moves with respect to the buoy frame.

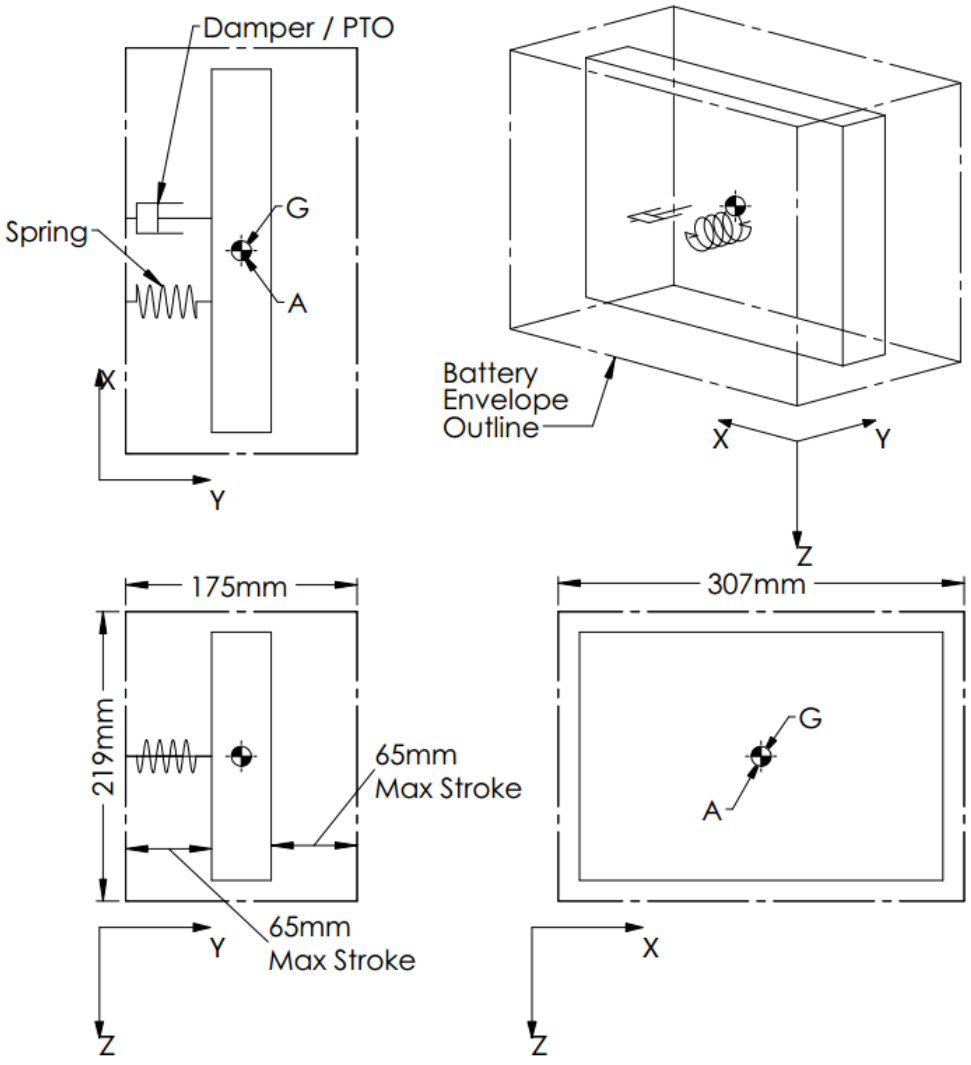

Figure 2.7 – Linear WECO with movement in the sway (Y) direction

2.2.2 Linear Z WECO

The linear Z WECO is constrained to move parallel to the Z axis of the buoy frame. The maximum amplitude of oscillation is 0.080m. A linear spring and PTO are shown, along with points *A* and *G*. Point *A* is the location of the oscillating mass at rest, and is stationary with respect to the buoy frame. Point *G* is the CoM of the WECO oscillating mass and moves with respect to the buoy frame.

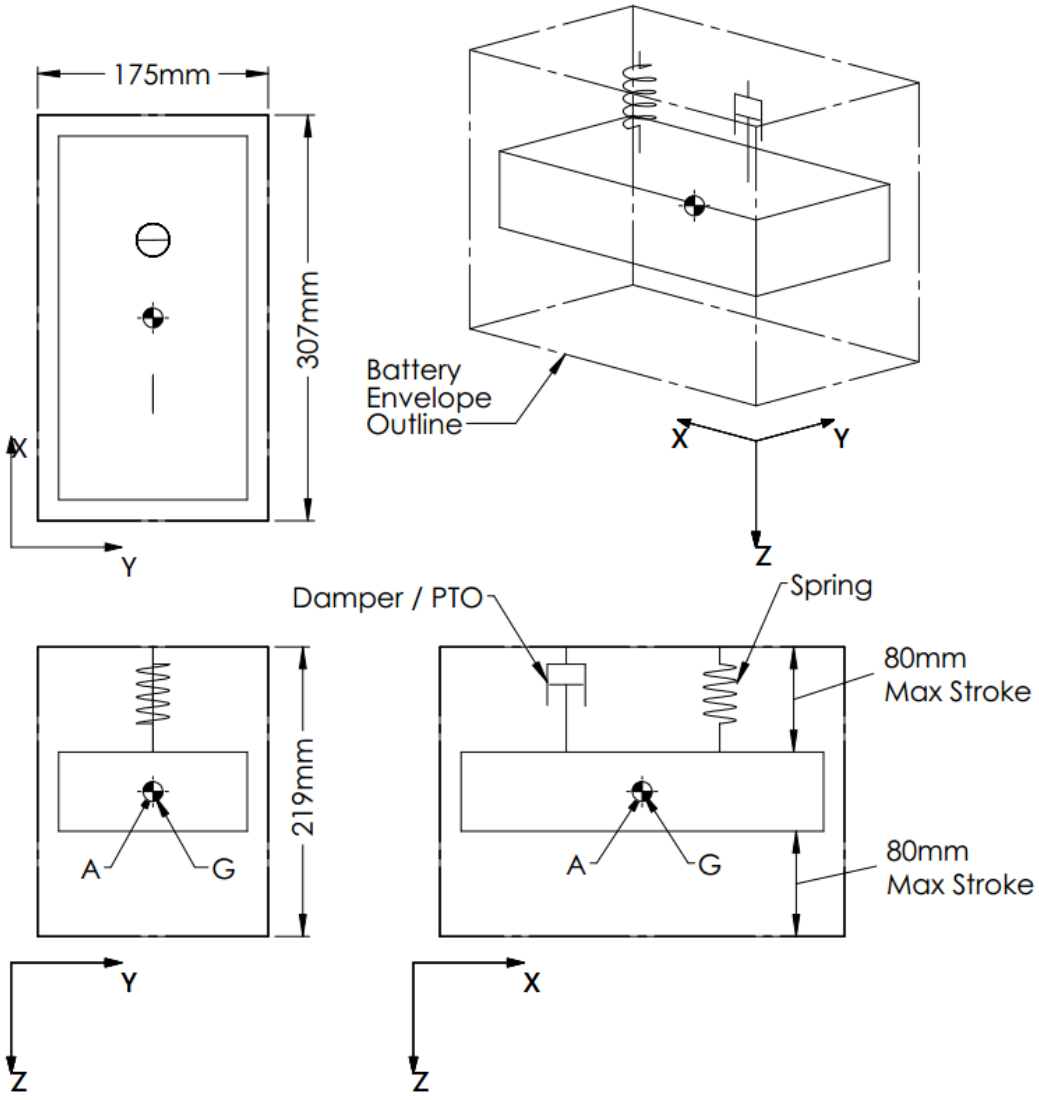

Figure 2.8 – Linear WECO with movement in the vertical (Z) direction

2.3 Closing

In this chapter, the TriAXYS buoy was described along with the physical constraints associated with the installation of a WECO. Two battery locations were identified as possible WECO locations. Five distinct WECO topologies were presented that could be installed in either battery location, resulting in 10 unique buoy/WECO configurations. The candidate WECOs consisted of two rotating devices and three translational devices. Each of the five candidates was designed to extract power from one of the surge, sway, heave, roll, and pitch DOFs of the TriAXYS buoy. Each candidate topology was investigated to find the maximum physical displacement that could be achieved with a 26 kg oscillating mass.

Chapter 3
Environmental Conditions

3.1 Overview of the Buoy Environment

Selection and application of the environmental conditions used to guide the design of the WECO is one of the most important inputs to the modeling process used in this work. Commonly, characteristic sea states are generated and applied to a hydrodynamic model of the buoy to determine the expected motion. The model must estimate the state dependent loads, such as mooring and buoyancy loads, based on the buoy and wave motions. It is difficult to create an accurate hydrodynamic model of the TriAXYS ODAS buoy, especially the mooring line. Instead of creating a model to approximate the state dependent loads, the approach taken in this work is to calculate a representative time history of external forces and moments from recorded buoy motions. Raw motion data was available from previous deployments of a TriAXYS buoy, and this data is used in this chapter to calculate the external loads that were applied to the buoy to impart this motion. These loads were then used as inputs for the evaluation of each candidate WECO configuration.

Motion data from a TriAXYS buoy installed off the coast of Ucluelet, BC, see Figure 3.1, was used to drive this process. This location was selected because it was exposed to open ocean swells, and is characteristic of where TriAXYS buoys are usually installed as part of wave resource assessment projects. Buoy motion throughout the winter months was the focus, as during summer months the buoy is expected to be entirely powered by solar irradiation. Data from the winters of 2014-2015, 2015-2016 was available in hourly 20 minute samples. This resulted in a total of 7207 datasets, each with a duration of 20 minutes, representing approximately 100 days of winter wave data.

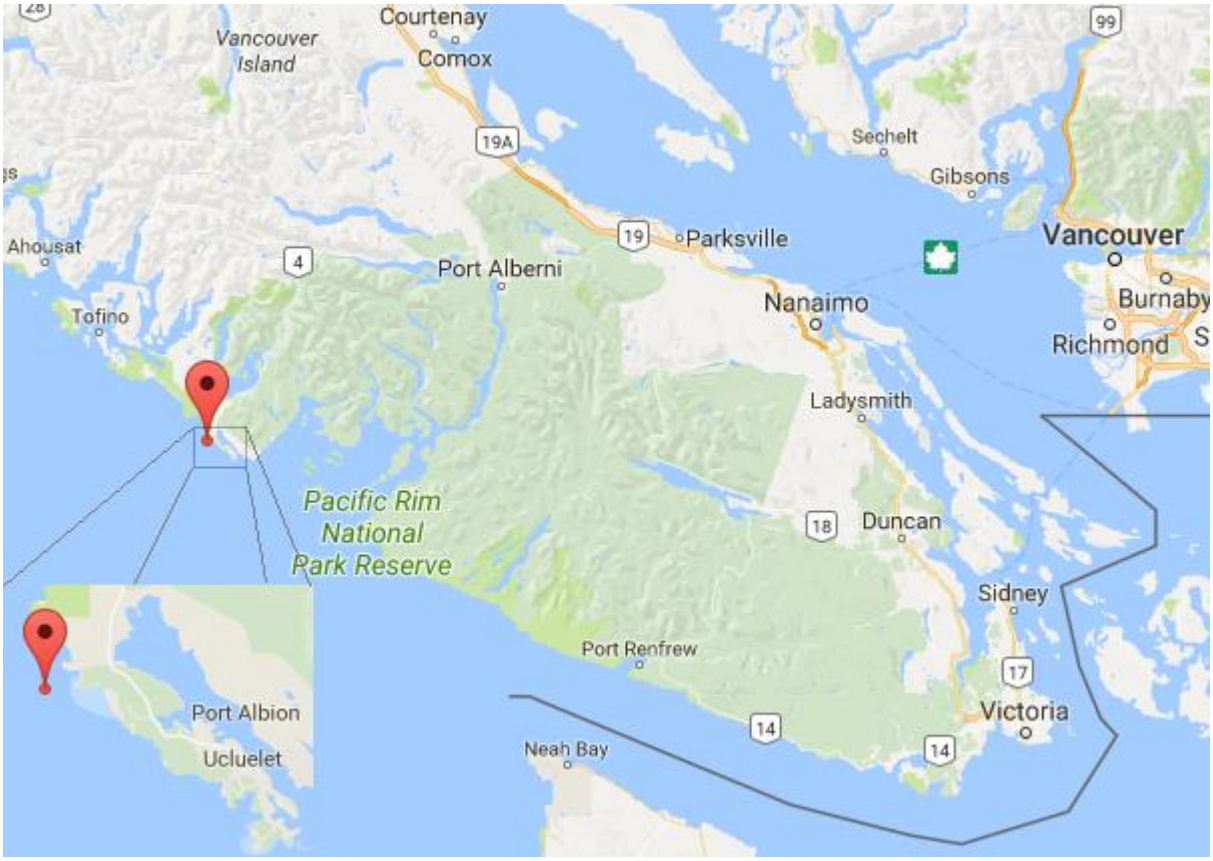

Figure 3.1 – Map of buoy location

3.2 Environmental Data Processing

TriAXYS buoys record raw accelerometer data in units of m/s^2, and rotational rate data in units of deg/s at a sampling frequency of 4 Hz. These sensors are mounted near the CoM of the buoy, and are aligned so that the data represents linear accelerations in the surge (X), sway (Y), and heave (Z) directions, and rotational rates in roll (about X), pitch (about Y), and yaw (about Z) rotations about the axes of the buoy fixed reference frame shown in Figure 2.4.

TriAXYS raw motion data is normally processed into wave information by the TriAXYS post processor. It calls on a proprietary algorithm, licensed from the National Research Council (NRC), written in the programming language FORTRAN. The algorithm conditions the raw data and calculates buoy motion and sea state data such as HNE (Heave, North, and East buoy motions), significant wave height, and wave spectrum data. As an intermediate step, the algorithm does calculate the linear and rotational displacements of the buoy, but it does not

output this data during standard use. Outputs from this algorithm have previously been tested and have proven to accurately convert buoy motion into wave data [30].

The FORTRAN code was deciphered, and the pertinent code snippets were rewritten in MATLAB so that the buoy accelerations and displacements with respect to the local buoy reference frame could be calculated from the raw accelerometer and rotational rate gyro data. Specifics of the conditioning can't be discussed here as they are part of a proprietary algorithm, but Figure 3.2 shows the accelerometer and rotational rate gyro data before and after conditioning. This data was recorded on March 1, 2016 at 2:00am. Only 50 seconds of the time series data was plotted for clarity. The Fast Fourier Transform (FFT) plots have been enlarged, as a result a few very large low frequency data points from the raw data are excluded.

Some of the conditioning of the data is readily apparent. The acceleration due to gravity has been removed which is most apparent in the heave accelerometer data. The data has been passed through a filter where some low frequency oscillations were removed from the data as shown in Figure 3.3. The yaw data was made up solely of low frequencies, and was relatively small in amplitude, and so the yaw loads were not applied to the models because it would not impart significant energy to the WECOs.

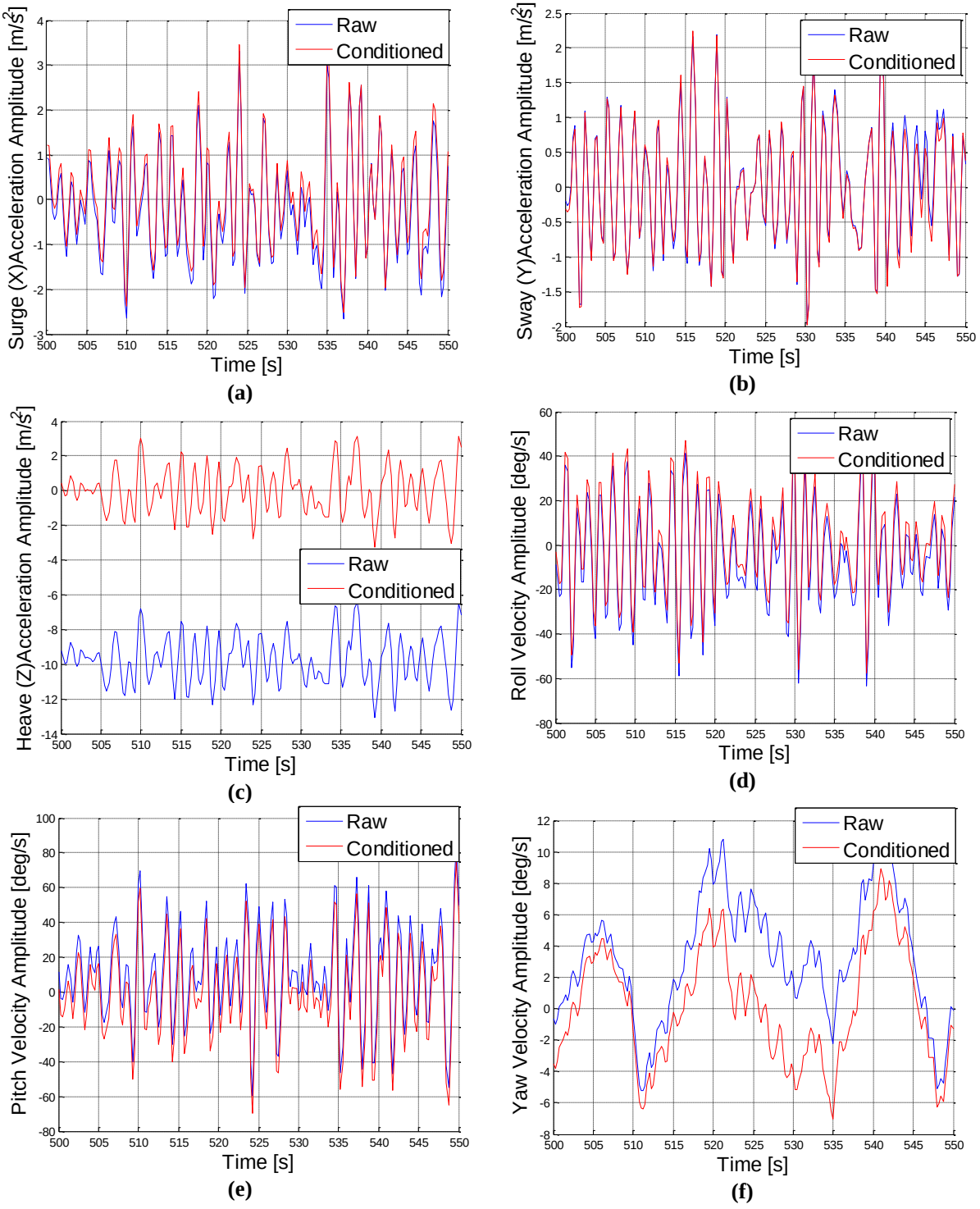

Figure 3.2 – Sample raw time series data before and after conditioning in (a) Surge acceleration (b) Sway acceleration (c) Heave acceleration (d) Roll velocity (e) Pitch velocity (f) Yaw velocity

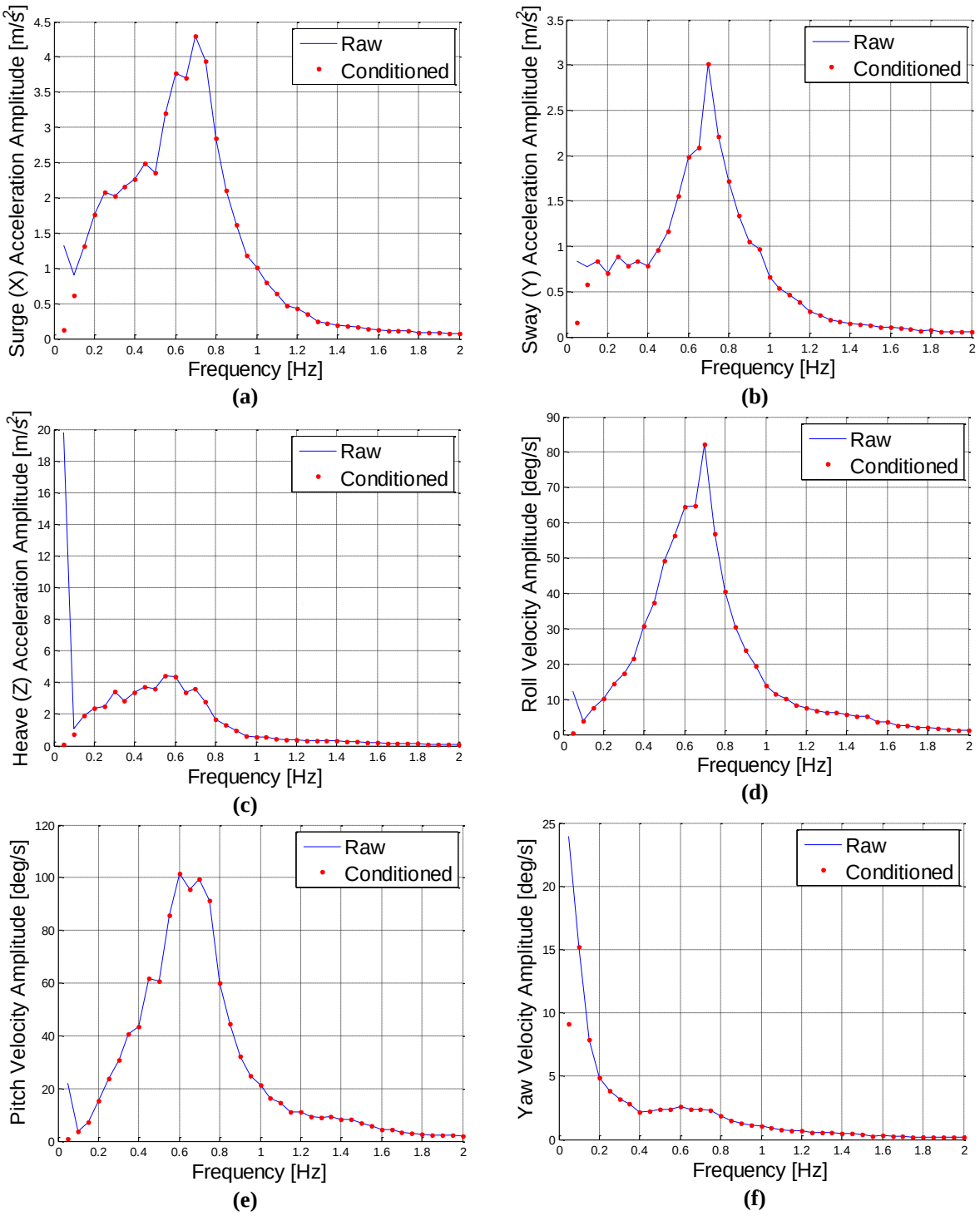

Figure 3.3 – Sample raw frequency data, raw and after conditioning in (a) Surge acceleration (b) Sway acceleration (c) Heave acceleration (d) Roll velocity (e) Pitch velocity (f) Yaw velocity

3.3 Buoy Loads and Associated Displacements

Acceleration and displacement data in each of the 6 DOFs with respect to the buoy frame of reference (Surge (X), Sway (Y), Heave (Z), Roll (R), Pitch (P), Yaw (W)) was calculated from the conditioned raw data. The raw linear accelerometer data was integrated twice to find the linear displacements. The raw rotational rate data was both integrated to find the rotational displacements, and differentiated to find the rotational accelerations. Integration and differentiation was completed in the frequency domain by scaling each amplitude with respect to its frequency.

The displacement data was used to compare the calculated motions to the original buoy motions, and as the initial conditions for the forward integration time based simulations, discussed in the next section. The acceleration data was used to calculate the external loads that were applied to the buoy to cause the recorded motions. These loads include all sources: waves, wind, mooring, etc.

The dynamic properties of the buoy were extracted from the TriAXYS 3D model. The accelerations were input to the 6 DOF equations of rigid body motion for the TriAXYS buoy to find the time series of average forces and moments that would have been required to move the buoy through is recorded motion

$$\bar{F}_i = m\,\bar{a}_i \; and \; \bar{T}_i = \underline{I}\,\dot{\bar{\omega}}_i + \bar{\omega}_{Buoy} \times (\underline{I}\,\bar{\omega}_{Buoy}) \tag{1}$$

where
- i = Timestep / datapoint
- $\bar{F}_i$ = The average force vector applied to the buoy CoM by the environment, over the timestep
- m = The mass of the original buoy with all batteries and no WECO installed
- $\bar{a}_i$ = The vector of average linear acceleration through the timestep
- $\bar{T}_i$ = The average moment vector applied to the buoy by the environment, over the timestep
- $\underline{I}$ = The inertia tensor of the original buoy about its CoM with all batteries and no WECO installed
- $\dot{\bar{\omega}}_i$ = The vector of average rotational accelerations through the timestep

3.4 Closing

In this chapter, the data used as inputs to this investigation were described. The methods for processing this data into usable loads and displacements with respect to the buoy frame were introduced. Buoy frame displacements are not a useful quantity outside this thesis, they are extracted from the original buoy rates for use as the initial conditions in the time domain simulations described in Chapter 4, and to validate the results of time domain simulations in Chapter 5. Further, the local frame displacements are necessary for the comparative analysis performed in Section 6.1.

Many of the external loads on the buoy are state dependant, so if the WECO significantly affected the motion of the buoy these loads would no longer be valid. This risk was accepted since one of the key constraints on the WECO was that it could not significantly affect the buoy motion, that could in turn alter the wave estimates, especially within the specified wave recording frequencies of 0.03-0.63 Hz. As such, if a viable candidate design is identified, the modeling method should apply, and the performance estimates generated will be valid.

Chapter 4
Equations of Motion

Chapter 3 presented the time histories of forces and moments that develop at the CoM of the buoy when it is subjected to winter swell conditions. In this chapter, these loads are applied to a dynamic model of each candidate WECO configuration to discover the resulting motion of both the buoy and the internal oscillating mass. The development of the various dynamic models is explained here. These models depict the candidate WECO configurations introduced in Chapter 2.

4.1 Physical Attributes of the Configurations

Each WECO configuration is a system of two rigid bodies connected by a spring and / or damper. One rigid body is the buoy with a battery removed in the location where the WECO was installed and including the 4kg mass representing the stationary components of the WECO. The other rigid body is the oscillating mass of the WECO. Key locations in the systems, along with associated physical properties, were defined so that the dynamic models for each configuration could be created. Table 4.1 summarizes these locations and properties.

Table 4.1 – Key locations and physical properties

Point *C*	≡	CoM of the buoy and WEC assembly, when the WECO oscillating mass displacement is zero (also the origin of the buoy frame of reference). The location at which the loads are applied to the models.
Point *G*	≡	CoM of the WECO mass
Point *B*	≡	CoM of the buoy without WECO (with the appropriate battery removed and the 4 kg block added)
Point *A*	≡	For linear WECOs, this is the location of the CoM of the WECO oscillating mass at rest For rotating WECOs, this is the location of the center of rotation of the WECO oscillating mass

$\underline{I}_{Buoy}$	≡	Inertia tensor of the TriAXYS buoy, about its CoM (point *B*) without a WECO installed (and with the appropriate battery removed)
m_{Buoy}	≡	Mass of the TriAXYS buoy without WECO (and with one battery removed)
m_{WECO}	≡	Mass of the WECO
$\underline{I}_{WECO}$	≡	Inertia tensor of the WECO mass, taken about its CoM (point *G*)

Three-dimensional CAD models were used to evaluate the physical characteristics of the various buoy and WECO configurations. Mass properties of the buoy were calculated with a battery removed from the location that the WECO would be installed, either location 1 or location 2, and the location of that CoM was labeled point *B*.

Due to the WECO designs being very similar in weight to the batteries, the location of point *C* in the buoy frame for all configurations, and also the CoM of the original buoy where the loads were evaluated, were within 10 mm of each other. Because this distance is small compared to buoy motions and to the diameter of the buoy, the loads that were evaluated at the original buoy CoM were applied directly at point *C* for each configuration without modification.

Mass properties were also calculated with the WECO installed and at rest, and the location of that CoM was labeled point *C*. This was the location at which the force and moment histories calculated in Chapter 3 were applied to each model. Motions of this point were compared to the motions of the original buoy CoM for during validation.

Point *A* was designated as the pivot point of the WECO oscillations for rotating types, and as the location of the CoM of the WECO mass when at rest for linear types. Point *G* was designated as the CoM of the WECO (Generator) oscillating mass.

Position vectors from point *C* to points *A* and *B* were determined using the 3D models for each buoy and WECO assembly. The value for each vector in each configuration was obtained from the 3D drawings.

A unit vector $\bar{f}_{PTO}$ was used to represent the direction of WECO motion with respect to the buoy frame of reference. For rotating WECOs this direction was parallel to the axis of rotation,

and for linear WECOs it was parallel to the direction of WECO translation. For rotating WECOs, it was also useful to define a unit vector aligned with the rotating arm $\bar{n}_{PTO}$, it is used in equation (12). This vector was always perpendicular to the corresponding $\bar{f}_{PTO}$.

Table 4.2 - WECO direction of motion unit vectors

WECO Design	**Unit Vector $\bar{f}_{PTO}$**
Rotating Short	$[1; 0; 0]$
Rotating Long	$[0; 1; 0]$
Linear X	$[1; 0; 0]$
Linear Y	$[0; 1; 0]$
Linear Z	$[0; 0; 1]$

Table 4.3 - Rotating WECO oscillating arm direction unit vectors

WECO Design	**Unit Vector $\bar{n}_{PTO}$**
Rotating Short	$[0; \cos\beta\,; \sin\beta]$
Rotating Long	$[\cos\beta\,; 0; \sin\beta]$

4.2 Lagrange Equation Development

The Lagrange method was used to develop the dynamic model of each candidate WECO configuration. These models were used in the time domain, forward integration simulations for a range of spring constants and damping coefficients.

The buoy frame of reference was used as the reference frame for developing the equations of motion since the force and moment time series calculated in Chapter 3 were evaluated in this frame. The origin of this reference frame was placed at the CoM of each buoy/WECO assembly, point *C*, as discussed in Section 4.1.

In addition to the Lagrange equations, Rayleigh's dissipation function was employed to evaluate the damping effects of the power take off system. The following is the general derivation of the equations of motion for the buoy and WECO assemblies.

The Lagrange / Rayleigh equations are

$$\frac{d}{dt}\left(\frac{\partial T}{\partial \dot{q}_j}\right) - \frac{\partial T}{\partial q_j} + \frac{\partial V}{\partial q_j} + \frac{\partial R}{\partial \dot{q}_j} = Q_j\,, \qquad j = 1,2,\dots,N \tag{2}$$

where Q_j = The generalized forces
T = The kinetic energy of the system
V = The potential energy of the system
R = Rayleigh's dissipation function
q_j = The independent kinematic variables that describe buoy and WECO location with respect to time

and q_1 = Surge displacement of point *C* with respect to the buoy frame
q_2 = Sway displacement of point *C* with respect to the buoy frame
q_3 = Heave displacement of point *C* with respect to the buoy frame
q_4 = Roll Displacement with respect to the buoy frame
q_5 = Pitch Displacement with respect to the buoy frame
q_6 = Yaw Displacement with respect to the buoy frame
q_7 = WECO Oscillating Mass Displacement (rotation or translation) with respect to the buoy frame

Kinetic Energy

The kinetic energy equations for the system were broken into that of the buoy (with the appropriate battery removed) in rotation and translation, and the WECO mass in rotation and translation. The total kinetic energy is

$$T = T_{rot\ Buoy} + T_{lin\ Buoy} + T_{rot\ WECO} + T_{lin\ WECO}$$

where each individual kinetic energy term was described as

$$T_{rot\,Buoy} = 1/2\,\bar{\omega}_{Buoy}^{T}\,\underline{I}_{Buoy}\,\bar{\omega}_{Buoy} \tag{3}$$

$$T_{lin\,Buoy} = 1/2\,\bar{v}_{B}^{T}\,m_{Buoy}\,\bar{v}_{B} \tag{4}$$

$$T_{rot\,WEC} = 1/2\,\left(\bar{\omega}_{Buoy} + \dot{\beta}\,\bar{\mathrm{f}}_{\mathrm{PTO}}\right)^{T}\bar{I}_{WECO}\left(\bar{\omega}_{Buoy} + \dot{\beta}\,\bar{\mathrm{f}}_{\mathrm{PTO}}\right)$$
note: for linear WECOs, $\dot{\beta} = 0$ and so $T_{rot\,WEC} = 1/2\,\left(\bar{\omega}_{Buoy}\right)^{T}\underline{I}_{WECO}\left(\bar{\omega}_{Buoy}\right)$ (5)

$$T_{lin\,WEC} = 1/2\,\bar{v}_{G}^{T}\,m_{WECO}\,\bar{v}_{G} \tag{6}$$

The velocity of the buoy (less one battery) CoM point *B* is

$$\bar{v}_{B} = \bar{v}_{C} + \bar{v}_{B/C} = \bar{v}_{C} + \bar{\omega}_{Buoy} \times \bar{r}_{B/C} \tag{7}$$

The velocity of the CoM of the WECO mass point *G* is

$$\begin{aligned}\bar{v}_{G} &= \bar{v}_{C} + \{\bar{v}_{A/C}\} + \{\bar{v}_{G/A}\} \\ &= \bar{v}_{C} + \{\bar{\omega}_{Buoy} \times \bar{r}_{A/C}\} + \{\bar{\omega}_{Buoy} \times \bar{r}_{G/A} + \dot{\bar{r}}_{G/A}\}\end{aligned} \tag{8}$$

The vector $\bar{r}_{G/A}$ varies with respect to time due to the displacement of the WECO with respect to the buoy; the terms generated by this variable resulted in unacceptable solution times in the order of weeks instead of days. Depending on the style of the WECO, rotating or linear, different simplifications were necessary to achieve a practical computation time, see Sections 4.2.1 and 4.2.2.

Potential Energy

The only potential energy included in the model was that contained in the spring connecting the WECO to the TriAXYS buoy. The datum for the spring is chosen so that the gravitational force on the WECO mass is offset when the displacement α or β is zero.

Potential energy due to elevation changes in the buoy and WECO configurations are not considered because gravitational and buoyancy loads are included in the forces and moments calculated in Chapter 3. The gravitational effects that would cause WECO motion due to the

changing alignment of the buoy with the force of gravity were ignored, because the actual orientation of the buoy during computations was not known, see Section 4.4. These oscillations would be very small and would have very little effect on power generation for any configuration.

$$V = \frac{1}{2} k_{Spring}\, \alpha^2 \qquad \text{Linear WECOs}$$
$$V = \frac{1}{2} k_{Spring}\, \beta^2 \qquad \text{Rotating WECOs} \tag{9}$$

Rayleigh's dissipation function

Rayleigh's dissipation function was applied to quantify the energy dissipated by the PTO unit

$$R = \frac{1}{2} c_{PTO}\, \dot{\alpha}^2 = \frac{1}{2} (c_{critical}\, \zeta) \dot{\alpha}^2 \qquad \text{Linear WECOs}$$
$$R = \frac{1}{2} c_{PTO}\, \dot{\beta}^2 = \frac{1}{2} (c_{critical}\, \zeta) \dot{\beta}^2 \qquad \text{Rotating WECOs} \tag{10}$$

4.2.1 Linear WECO Simplifications

The cross product $\bar{\omega}_{Buoy} \times \bar{r}_{G/A}$ in (8) accounts for changes in the velocity imposed on point *G* by buoy rotation, when the WECO is somewhere other than at rest (i.e. when the displacement α was zero, the vector $\bar{r}_{G/A}$ was zero and this term was also zero). Since the maximum displacement of the WECO is small, this term is also small, and so it was set to zero for all WECO positions.

The resulting absolute velocity of point *G* for linear WECOs is

$$\begin{aligned} \bar{\mathrm{v}}_{\mathrm{G}} &= \bar{\mathrm{v}}_{\mathrm{C}} + \{\bar{\omega}_{Buoy} \times \bar{r}_{A/C}\} + \{\bar{\omega}_{Buoy} \times \bar{r}_{G/A}|_{\alpha=0} + \dot{\bar{r}}_{G/A}\} \\ &= \bar{\mathrm{v}}_{\mathrm{C}} + \{\bar{\omega}_{Buoy} \times \bar{r}_{A/C}\} + \{\dot{\bar{r}}_{G/A}\} \end{aligned} \tag{11}$$

where $\bar{r}_{G/A}|_{\alpha=0} = 0\, \bar{\mathrm{f}}_{\mathrm{PTO}} = [0; 0; 0]$

$\dot{\bar{r}}_{G/A} = \dot{\alpha}\, \bar{\mathrm{f}}_{\mathrm{PTO}}$

4.2.2 Rotating WECO Simplifications

For rotating WECOs, the vector $\bar{r}_{G/A}$ includes the length of the oscillating pendulum at rest, along with any change due to WECO rotation. Similarly to the simplification for linear WECOs, the change in $\bar{r}_{G/A}$ due to WECO motion was removed from the calculation of the cross-product term $\bar{\omega}_{Buoy} \times \bar{r}_{G/A}$ in (8). The small angle theorem was also applied to the vector $\bar{r}_{G/A}$ in (13) before differentiation in (14), so that the computation time was practical.

Equation (12) shows the complete equation for $\bar{r}_{G/A}$ and is followed by the approximations after applying the small angle theorem for each rotating WECO. Equation (13) shows the evaluation of this vector at rest (with β=0), and (14) shows the evaluation of the rate of change of this vector for both short and long rotating WECOs.

$$\bar{r}_{G/A} = L\,\bar{\mathrm{n}}_{\mathrm{PTO}} \tag{12}$$

$$= [0; \mathrm{L}\cos\beta\,; \mathrm{L}\sin\beta] \cong [0; \mathrm{L}; \mathrm{L}\,\beta] \quad \text{Short WECO}$$

$$= [\mathrm{L}\cos\beta\,; 0; \mathrm{L}\sin\beta] \cong [\mathrm{L}; 0; \mathrm{L}\,\beta] \quad \text{Long WECO}$$

$$\bar{r}_{G/A}|_{\beta=0} = [0\,; L\,;\, 0] \quad \text{Short WECO} \tag{13}$$

$$= [\mathrm{L}\,; 0\,;\, 0] \quad \text{Long WECO}$$

$$\dot{\bar{r}}_{G/A} = \frac{d}{dt}[0\,;\, L\,;\, L\,\beta] \text{ or } \frac{d}{dt}[\mathrm{L}; 0; \mathrm{L}\,\beta] \tag{14}$$

$$= [0\,;\, 0\,;\, L\,\dot{\beta}] \quad \text{Short and Long WECOs}$$

The resulting absolute velocity of point *G* for rotating WECOs is

$$\bar{v}_G = \bar{v}_C + \{\bar{\omega}_B \times \bar{r}_{\mathrm{A/C}}\} + \{\bar{\omega}_B \times \bar{r}_{G/A}|_{\beta=0} + \dot{\bar{r}}_{G/A}\} \tag{15}$$

4.3 Physical Parameter Values

Following are the constant values for certain terms for each WECO configuration. The mass of the buoy with one battery removed and the 4 kg block installed to represent the PTO and other stationary parts of the WECO was 178.7 kg.

For simplicity in the linear WECOs, the same WECO mass and 4 kg block location was used to develop each of the following values. There was very little difference between these values for each linear WECO.

Table 4.4 – Values of the vector $\bar{r}_{A/C}$ for each configuration

Location 1, short rotating WECO	$\bar{r}_{A/C} = [139.5;\ -66.5;\ -0.40]$	mm
Location 2, short rotating WECO	$\bar{r}_{A/C} = [153.5;\ -41.6;\ 66.6]$	mm
Location 1, long rotating WECO	$\bar{r}_{A/C} = [-108.2;\ 181.6;\ 68.3]$	mm
Location 2, long rotating WECO	$\bar{r}_{A/C} = [45.1;\ 0.35;\ 68.4]$	mm
Location 1, linear WECO	$\bar{r}_{A/C} = [0.40;\ 181.1;\ 68.1]$	mm
Location 2, linear WECO	$\bar{r}_{A/C} = [153.3;\ 0.35;\ 68.2]$	mm

Table 4.5 – Values of the vector $\bar{r}_{B/C}$ for each configuration

Location 1, short rotating WECO	$\bar{r}_{B/C} = [-0.058;\ -32.7;\ -9.7]$	mm
Location 2, short rotating WECO	$\bar{r}_{B/C} = [-22.5;\ -6.3;\ -9.8]$	mm
Location 1, long rotating WECO	$\bar{r}_{B/C} = [-9.1;\ -26.3;\ -9.9]$	mm
Location 2, long rotating WECO	$\bar{r}_{B/C} = [-31.4;\ -0.051;\ -9.9]$	mm
Location 1, linear WECO	$\bar{r}_{B/C} = [-0.058;\ -26.8;\ -10.1]$	mm
Location 2, linear WECO	$\bar{r}_{B/C} = [-22.7;\ -0.051;\ -10.1]$	mm

Table 4.6 – Values of the mass moment of inertia of the WECO mass for each configuration

Short rotating WECO	$\underline{I}_{WEC} = \begin{bmatrix} 0.0438 & 0 & 0 \\ 0 & 0.1985 & 0 \\ 0 & 0 & 0.1744 \end{bmatrix}$	$kg\,m^2$
Long rotating WECO	$\underline{I}_{WEC} = \begin{bmatrix} 0.0635 & 0 & 0 \\ 0 & 0.0923 & 0 \\ 0 & 0 & 0.1075 \end{bmatrix}$	$kg\,m^2$
Linear WECOs	$\underline{I}_{WEC} = \begin{bmatrix} 0.0446 & 0 & 0 \\ 0 & 0.1472 & 0 \\ 0 & 0 & 0.1563 \end{bmatrix}$	$kg\,m^2$

Table 4.7 – Values of the mass moment of inertia of the buoy with one battery removed and the 4 kg block in place for each configuration

Location 1, short rotating	$\underline{I}_{Buoy} = \begin{bmatrix} 13.79 & -0.0023 & 0.0026 \\ -0.0023 & 14.70 & -0.3698 \\ 0.0026 & -0.3698 & 15.95 \end{bmatrix}$	$kg\,m^2$
Location 2, short rotating	$\underline{I}_{Buoy} = \begin{bmatrix} 14.82 & -0.0339 & -0.2987 \\ -0.0339 & 14.00 & -0.0179 \\ -0.2987 & -0.0179 & 16.28 \end{bmatrix}$	$kg\,m^2$
Location 1, long rotating	$\underline{I}_{Buoy} = \begin{bmatrix} 13.83 & -0.1190 & -0.0013 \\ -0.1190 & 14.74 & -0.4284 \\ -0.0013 & -0.4284 & 16.08 \end{bmatrix}$	$kg\,m^2$
Location 2, long rotating	$\underline{I}_{Buoy} = \begin{bmatrix} 14.78 & -0.0027 & -0.3637 \\ -0.0027 & 13.84 & -0.0044 \\ -0.3637 & -0.0044 & 16.14 \end{bmatrix}$	$kg\,m^2$
Location 1, linear	$\underline{I}_{Buoy} = \begin{bmatrix} 13.83 & -0.0022 & 0.0025 \\ -0.0022 & 14.67 & -0.4284 \\ 0.0025 & -0.4284 & 16.01 \end{bmatrix}$	$kg\,m^2$
Location 2, linear	$\underline{I}_{Buoy} = \begin{bmatrix} 14.78 & -0.0025 & -0.3598 \\ -0.0025 & 13.98 & -0.0044 \\ -0.3598 & -0.0044 & 16.27 \end{bmatrix}$	$kg\,m^2$

Table 4.8 – Values of the mass for the WECO oscillating mass for each design

Short rotating	$m_{WECO} = 26.1$	kg
Long rotating	$m_{WECO} = 25.9$	kg
Linear	$m_{WECO} = 26.4$	kg

4.4 Time Domain Modelling and Simulation

A MATLAB program was created that accepts inputs of the WECO configuration, and spring and damping rates, selects the corresponding set of physical parameters from Section 4.3, and populates the Lagrange equations for that configuration to generate the equations of motion.

Equations (3) and (4) are populated with data from Section 4.3 to form the kinetic energy of the buoy with the correct battery removed. The version of (5) that corresponds to the WECO being modeled is selected, and the appropriate simplifications to the WECO mass velocity in equation (6) are applied from equations (11) and (15). Equations (5) and (6) are populated with data from Section 4.3 to form the kinetic energy of the WECO mass. The potential energy (9) and Rayleigh's (10) equations are populated with the selected spring rate and damping coefficients. The Lagrange/Rayleigh equation (2) is then solved to find the equations of motion for each configuration.

A program was written in MATLAB for each WECO configuration and spring and damping rate, that called the program above to assemble the equations of motion and form the model for simulation. The appropriate subset of loads and initial conditions calculated in Section 3.3 was selected, depending on the goal of the simulation as described in Sections 6.1 and 6.2, and the Lagrange/Rayleigh equations were numerically integrated forward in time to find the resulting displacements of each configuration. A similar simulation program integrated the 6 DOF rigid body equations forward in time with the calculated loads, to find the simulated original buoy motions plotted in 5.2. For all models, the first two buoy displacements for the corresponding dataset were used as the initial conditions for the time domain simulations.

4.5 Processing of Results

During the time domain simulations described in Section 4.4, low frequency oscillations were imparted in the buoy motions. It is unknown exactly why these occurred, but are likely due the discontinuous application of the loads incorrectly representing the continuous loads they are meant to replace. There was also often an underlying constant velocity component in the simulated displacements. All results from the simulations were first detrended and then high pass filtered with a cut-off frequency equal to the minimum wave frequency that is measured by the TriAXYS, 0.03 Hz. This provided suitable data to be used for comparing displacements and finding power generation potential.

Power estimation

After the models were run, the average estimated power generated through the PTO was calculated for each dataset of loads. The instantaneous power at each data point was found, and the mean of those instantaneous powers was taken to estimate the average power generated throughout each 20 minute dataset, see (16)

$$P = \sum_1^M \frac{\dot{\alpha_i}^2 \, c_{PTO}}{M} = \sum_1^M \frac{\dot{\alpha_i}^2 \, c_{critical} \, \zeta}{M} \qquad \text{Linear WECOs}$$
$$P = \sum_1^M \frac{\dot{\beta_i}^2 \, c_{PTO}}{M} = \sum_1^M \frac{\dot{\beta_i}^2 \, c_{critical} \, \zeta}{M} \qquad \text{Rotating WECOs} \tag{16}$$

where $\dot{\alpha}_i \; or \; \dot{\beta}_i$ = The average WECO velocity through each datastep

M = The number of data points in the dataset

$c_{critical}$ = The critical damping coefficient if the buoy was held still and the WECO given an initial impulse

= $2 \cdot \sqrt{k_{Spring} \, m_{WECO}}$ for linear WECOs, and

$2 \cdot \sqrt{k_{Spring} \, I_{WECO}}$ for rotating WECOs

ζ = The damping ratio

4.6 Closing

In this chapter, the development of the models used in the time domain simulations was reviewed. The frame of reference was selected to be the CoM of each configuration, that was within 10 mm of the original buoy CoM. These two CoMs were defined as point *C*, and was considered to be in the same location of the buoy when developing the models, and for the following model validation in Chapter 5. This allowed for the loads to be applied at the same location that they were calculated from, and for direct comparison of the displacements during validation.

Other key locations were listed, including:

- Point *B*: The CoM of the buoy with one battery removed and the 4 kg block installed
- Point *A*: The center of rotation of the rotating WECO masses, aligned with its CoM, or the location of CoM of the translated WECO masses at rest (stationary in the buoy frame)
- Point *G*: The CoM of the WECO mass (moves in the buoy frame)

The Lagrange/Rayleigh equations were discussed, along with the description of the state variables of displacements in each of the 6 DOFs of motion for the buoy, and the single DOF of motion of the WECO mass. The simplifications associated with each type of WECO, rotating or translational, were outlined, and the physical parameter values for each configuration were listed in Section 4.3.

The methods used to populate the Lagrange/Rayleigh equations and create the models used in time domain simulations was introduced, along with the model used to simulate the motion of the original TriAXYS buoy when subjected to the calculated load histories.

Outputs from the simulations required processing by detrending and applying a high-pass filter to the displacement data. The equations used to calculate the theoretical power extracted from the PTO were presented.

Chapter 5
Dynamic Model Validation

5.1 Model Validation Overview

A two-step process was used to evaluate different sections of the MATLAB dynamic model that represented the buoy and WECO assembly. Each model was numerically integrated forward in time using MATLAB. For each validation step the computed motion of point *C*, the CoM of the buoy/WECO assembly described in Section 4.1, was compared to the original recorded buoy motion for the same time period.

1. In the first validation step, see Section 5.2, a MATLAB model of the original buoy was created and subjected to the calculated buoy loads.
2. For the second validation step, see Section 5.3, the model was expanded to include the WECO system, but with the spring rate set high enough that virtually no relative motion occurred between the buoy and the WECO. The dynamics of the buoy with a locked WECO would be nearly identical to the original buoy, and should result in the same motion from applying the calculated buoy loads.

These validations were performed using the 27 data sets selected using the IEC TC-114 Hs-Te histogram approach described in Chapter 6. This provides results from a representative cross section of loading frequencies. The simulated and recorded oscillation amplitudes of the displacements in each DOF are normalized by the associated significant wave height. The standard deviation between recorded and simulated amplitudes in each of 20 frequency bins between 0.1 and 2 Hz are calculated. The average oscillation amplitudes for the 27 datasets are plotted with the standard deviation shown as error bars on the original data curve.

5.2 Model Validation - Original Buoy

The first step in validating the MATLAB model was to apply a selection of load time series to a model of the original buoy. The displacement outputs from this simulation were compared to the buoy motion that was used to generate that same selection of load time series, and are shown in Figure 5.1. These plots show the average amplitudes across the 27 datasets, normalized by the associated significant wave height, and include error bars indicating the standard deviation. This

tested the application of the load time series and checked that the selection of the frames of reference and derivation of the Lagrange equations was correct.

The time series plots in Figure 5.2 show the displacements for the simulated buoy following the original buoy displacements very well. This gives confidence that the buoy is still following a similar path and so the loads remain valid, even if there are discrepancies in the amplitudes at certain frequencies as mentioned above.

The Pearson correlation coefficients (r values) for the displacement data in each DOF, for each of the 27 datasets are shown in Table 5.1. The minimum r value for all 135 time series plots was 0.95, indicating a very close correlation of the buoy displacement time series data.

Table 5.1 - Pearson correlation coefficients for the original and simulated buoy motion

Dataset	1	2	3	4	5	6	7	8	9	10	11	12	13	14
Suge	1.00	1.00	1.00	0.99	1.00	1.00	1.00	1.00	1.00	1.00	1.00	1.00	1.00	1.00
Sway	1.00	1.00	0.99	1.00	1.00	1.00	1.00	0.99	1.00	1.00	1.00	1.00	1.00	1.00
Heave	1.00	1.00	1.00	1.00	1.00	1.00	1.00	1.00	1.00	1.00	1.00	1.00	1.00	1.00
Roll	1.00	0.98	1.00	1.00	1.00	0.95	0.99	1.00	0.99	1.00	0.99	1.00	1.00	0.99
Pitch	0.99	1.00	1.00	0.99	0.99	0.95	1.00	1.00	1.00	0.98	1.00	1.00	1.00	0.99
Dataset	**15**	**16**	**17**	**18**	**19**	**20**	**21**	**22**	**23**	**24**	**25**	**26**	**27**	
Suge	1.00	1.00	1.00	1.00	1.00	1.00	1.00	1.00	1.00	1.00	1.00	1.00	1.00	
Sway	1.00	1.00	1.00	1.00	0.99	1.00	1.00	1.00	1.00	0.99	1.00	1.00	1.00	
Heave	1.00	1.00	1.00	1.00	1.00	1.00	1.00	1.00	1.00	1.00	1.00	1.00	1.00	
Roll	1.00	1.00	1.00	0.96	1.00	1.00	1.00	0.98	0.97	0.99	0.99	1.00	1.00	
Pitch	1.00	1.00	1.00	1.00	1.00	0.98	1.00	1.00	1.00	0.99	1.00	1.00	0.99	

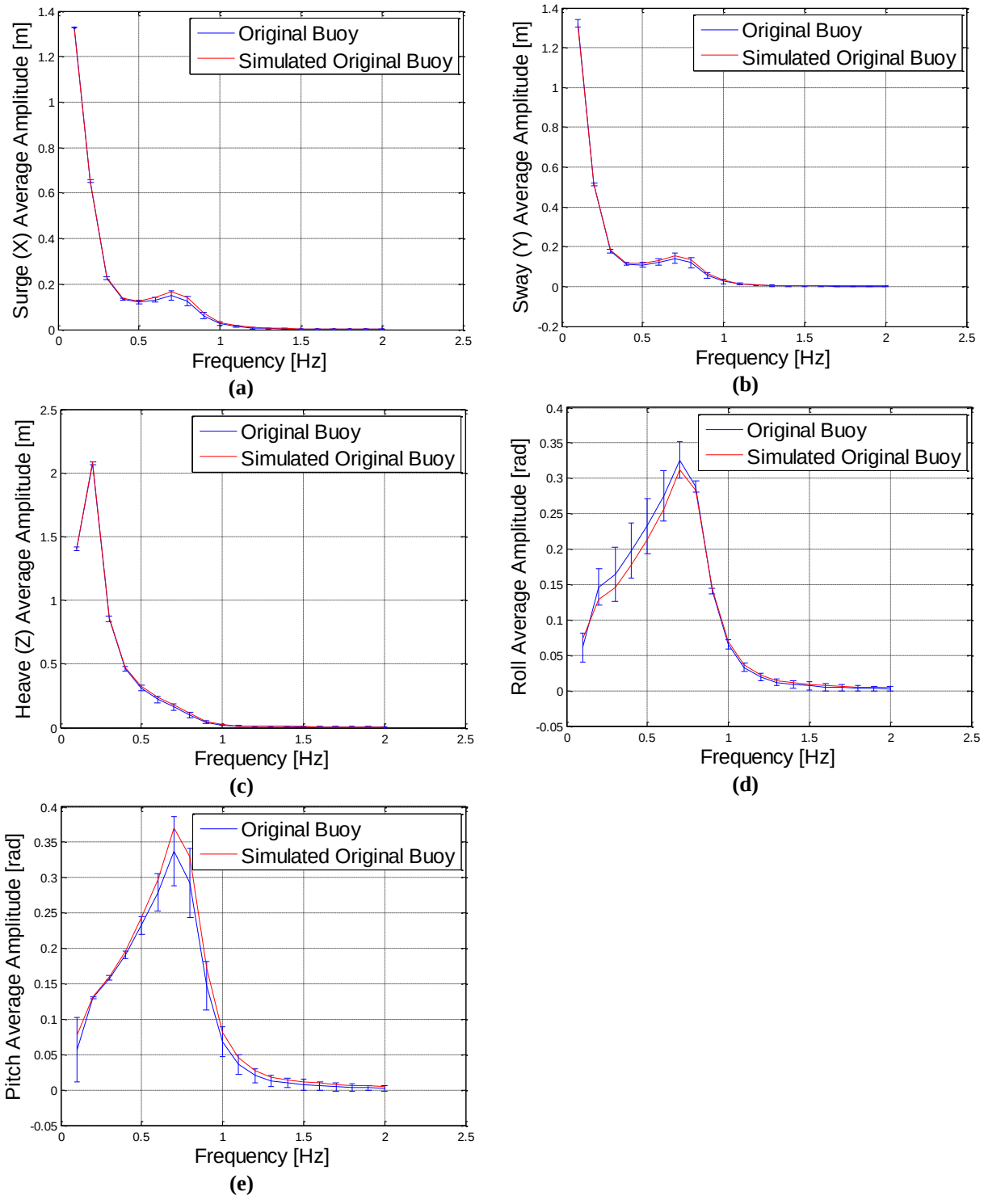

Figure 5.1 – Comparison plots of the original buoy motion and the simulated buoy motion in (a) Surge (b) Sway (c) Heave (d) Roll (e) Pitch

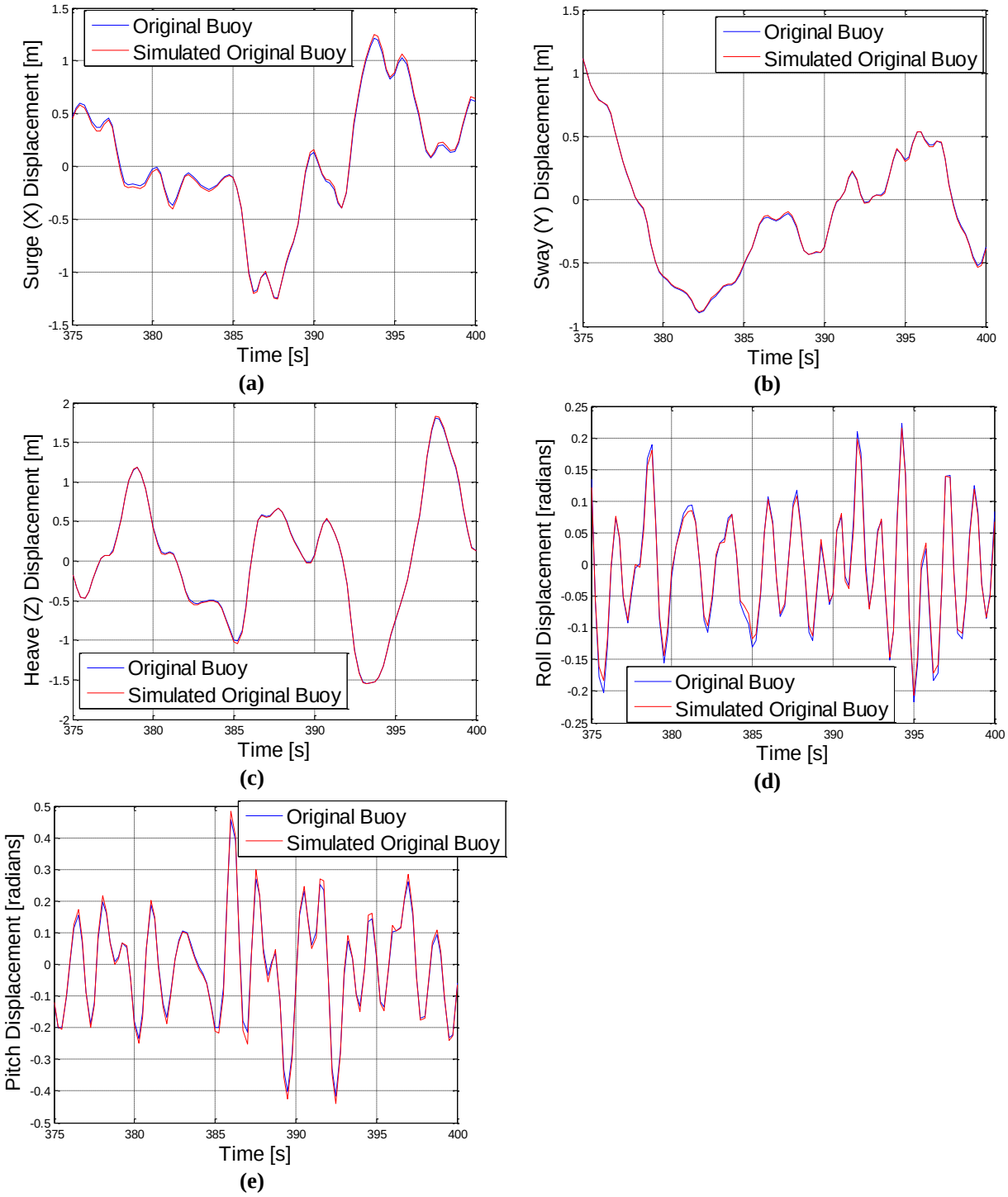

Figure 5.2 – Sample displacement comparison time domain plots of the original buoy motion and the simulated original buoy motion in (a) Surge (b) Sway (c) Heave (d) Roll (e) Pitch

5.3 Model Validation – Locked WECO

The next validation step was completed by removing one battery from the buoy and replacing it with a WECO with an extremely high spring constant. This emulated the WECO being locked in place. This way the buoy and WECO assembly would have similar dynamic attributes to the original buoy and should move through very similar motions when acted on by the same loads, even though the dynamic equations have moved from a single rigid body to a multi-body set of equations. Comparing the output displacements of the locked WECO model with the original buoy motion validated the dynamic coupling of the TriAXYS buoy and WECO in the motion equations. Validation tests were completed for each WECO configuration, the results from the linear WECO moving in the X direction installed in location 1 are shown in Figure 5.3. The error bars represent the standard deviation in each frequency bin for the 27 datasets.

Differences in the frequency plots of Figure 5.3 are very similar to those in Section 5.2. The time series plots in Figure 5.4 show the displacements for the buoy with the WECO locked out following the original buoy displacements very well. This gives confidence that the buoy is still following a similar path and so the loads remain valid, even if there are discrepancies in the amplitudes at certain frequencies as mentioned above.

The Pearson correlation coefficients (r values) are shown in Table 5.2. The minimum r value for all 135 time series plots was 0.95, indicating a very close correlation of the buoy displacement time series data.

Table 5.2 - Pearson correlation coefficients for the original and WECO locked buoy motion

Dataset	1	2	3	4	5	6	7	8	9	10	11	12	13	14
Surge	1.00	1.00	1.00	0.99	1.00	1.00	1.00	1.00	1.00	1.00	1.00	1.00	1.00	1.00
Sway	1.00	1.00	0.99	1.00	1.00	1.00	1.00	0.99	1.00	1.00	1.00	1.00	1.00	1.00
Heave	1.00	1.00	1.00	1.00	1.00	1.00	1.00	1.00	1.00	1.00	1.00	1.00	1.00	1.00
Roll	1.00	0.98	1.00	1.00	1.00	0.95	0.99	1.00	0.99	1.00	0.99	1.00	1.00	0.99
Pitch	0.99	1.00	1.00	0.99	0.99	0.95	1.00	1.00	1.00	0.98	1.00	1.00	1.00	0.99
Dataset	**15**	**16**	**17**	**18**	**19**	**20**	**21**	**22**	**23**	**24**	**25**	**26**	**27**	
Surge	1.00	1.00	1.00	1.00	1.00	1.00	1.00	1.00	1.00	1.00	1.00	1.00	1.00	
Sway	1.00	1.00	1.00	1.00	0.99	1.00	1.00	1.00	1.00	0.99	1.00	1.00	1.00	
Heave	1.00	1.00	1.00	1.00	1.00	1.00	1.00	1.00	1.00	1.00	1.00	1.00	1.00	
Roll	1.00	1.00	1.00	0.96	1.00	1.00	1.00	0.98	0.97	0.99	0.99	1.00	1.00	
Pitch	1.00	1.00	1.00	1.00	1.00	0.98	1.00	1.00	1.00	0.99	1.00	1.00	0.99	

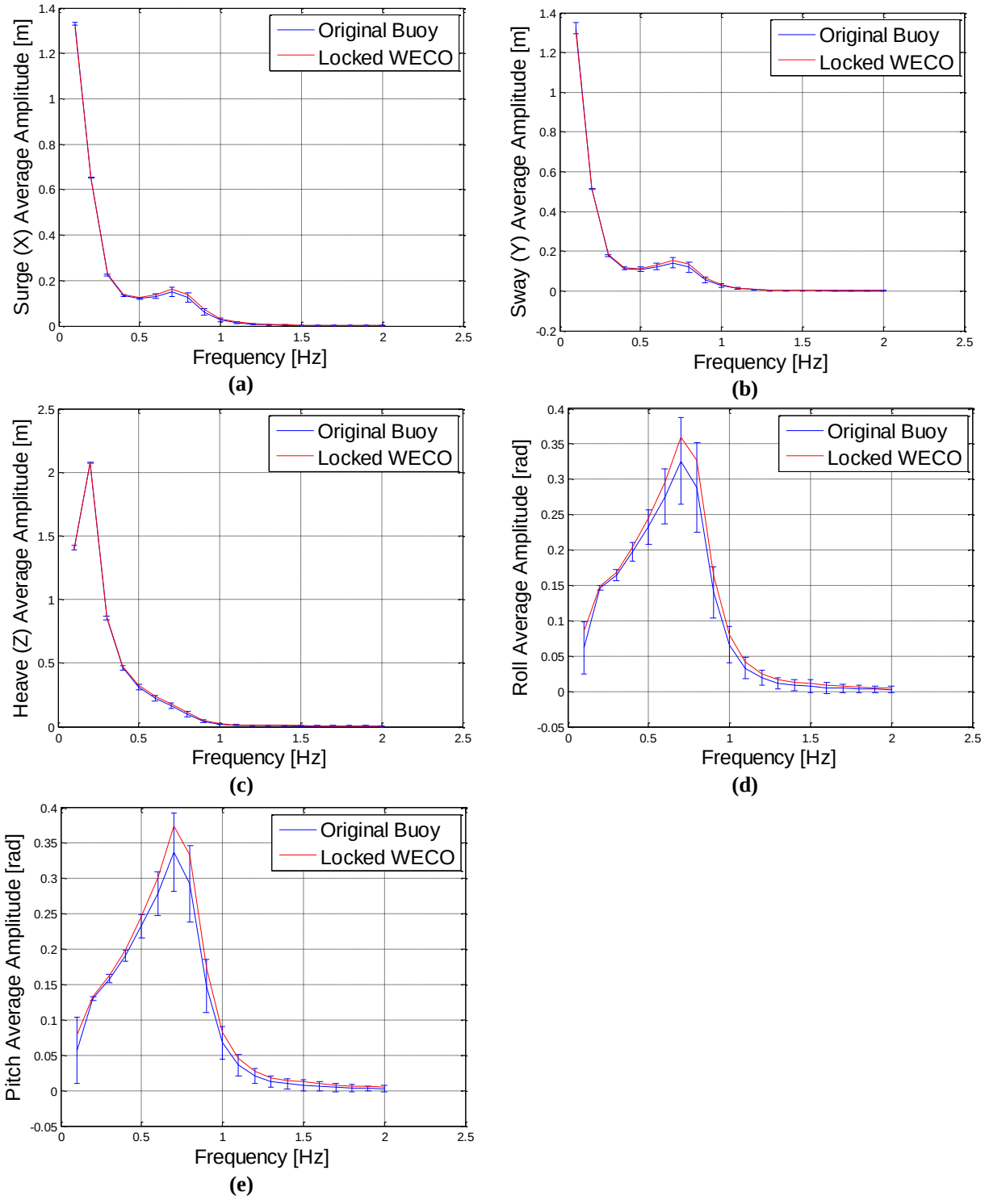

Figure 5.3 – Comparative plots of the original buoy motion and simulated motion of the buoy and WECO with an extremely stiff spring in (a) Surge (b) Sway (c) Heave (d) Roll (e) Pitch

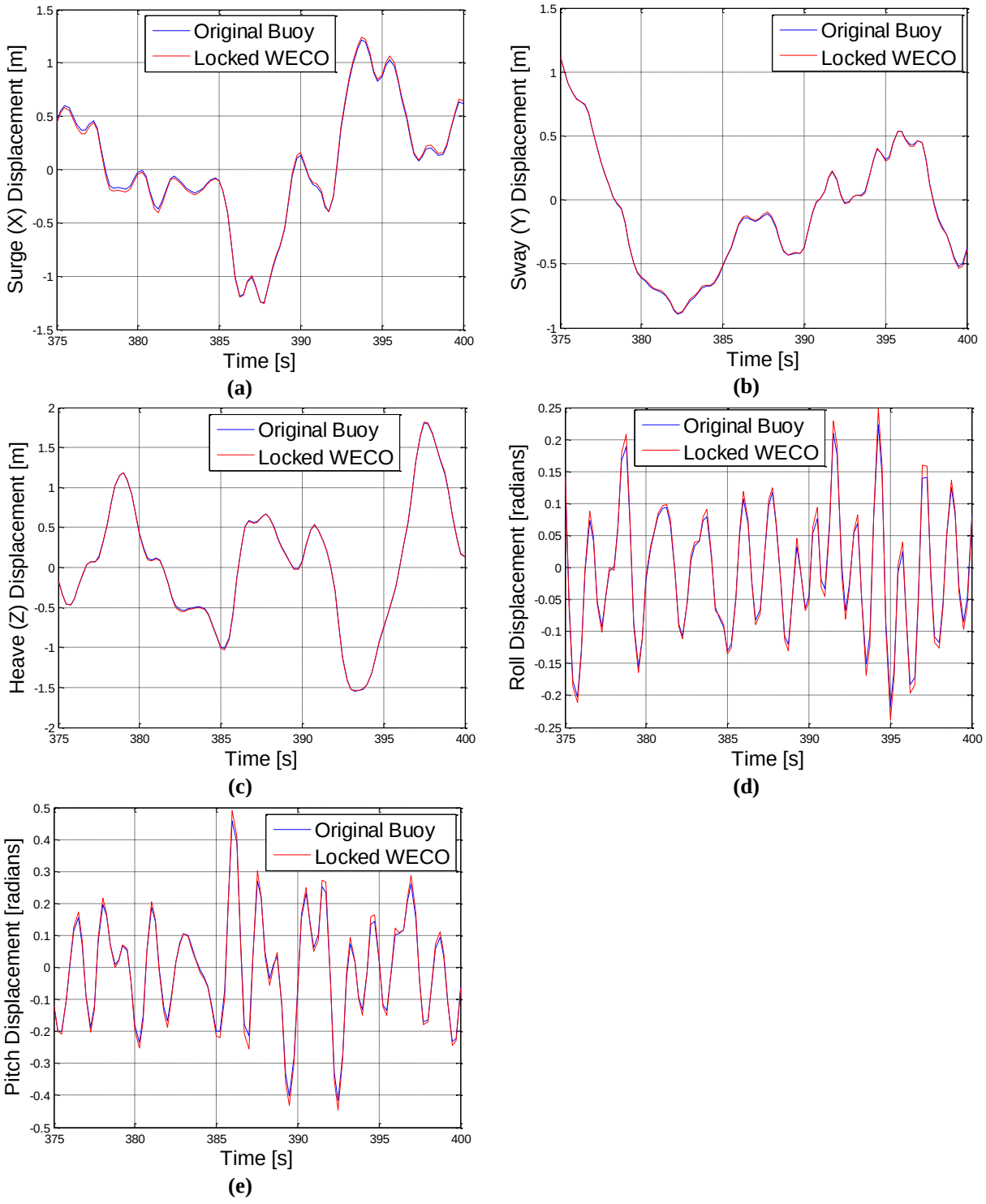

Figure 5.4 – Sample displacement comparison time domain plots of the original buoy motion and the buoy motion with a locked WECO in (a) Surge (b) Sway (c) Heave (d) Roll (e) Pitch

5.4 Closing

In this chapter the methods used to validate the models that were developed in Chapter 4 were applied. All models were deemed valid, with minimal discrepancies between the original buoy displacements, and simulated displacements of the original buoy. The new multi-body dynamic equations were validated by locking the WECO masses in place with an extremely high spring rate, and the output displacements were very close to the original buoy. The displacements calculated by the rigid body model for the original buoy, and the displacements output by simulating the multi-body WECO configuration models with extremely high spring rates, correlated very well with the displacements that were calculated from the rate data recorded by the original buoy.

In the next chapter, the spring rate is lowered so that the WECO mass oscillates, and the configurations that generate the highest theoretical power output are selected along with the associated spring rate and damping coefficient pairs.

Chapter 6
WECO Design Analysis

Having validated the dynamic models of the WECO configurations in the previous chapter, the models are now employed to calculate expected power outputs through the winter months. In Section 6.1, WECO configurations are compared on the basis of a theoretical ceiling of average winter power generation, with spring rates tuned to the loading frequency and the damping ratio optimized for power output, and the most promising designs are identified. In Section 6.2, the most promising designs are evaluated to estimate their realistic average winter power generation, with a static spring rate and damping ratio, that is of course lower than the theoretical ceiling used for the comparative analysis.

6.1 Comparative Analysis of all WECO Configurations

Five WECO designs were analyzed in two buoy locations, for a total of 10 unique Buoy/WECO configurations. To determine the configuration most likely to generate the greatest power through the winter months, a subset of buoy load datasets were applied to each model to find a theoretical ceiling of the average power that could be generated through the winter months, so that the WECO configurations could be compared on a level ground. This was done by tuning the spring rates and damping ratios to the applied loads, this method is described in more detail later in this section.

An accepted approach, developed and specified by the International Electrotechnical Commission Technical Committee 114 (IEC TC 114) [31], for estimating WEC power generation over an extended time period is to form groupings of similar wave states, and assume that the power output for all wave states in a group will average out to the wave state closest to the center of the group. These groupings were developed based on Hs (Significant Wave Height) and Te (Energy Period) values for each 20 minute sample. This works well for WEC/WECOs harvesting energy from vertical motion, but may not properly estimate the average power output from WEC/WECOs harvesting energy from other directions (surge, pitch, etc.). Since some of the WECOs being analyzed in this thesis were more sensitive to directions of motion other than heave induced motion, the wave states representing the significant motions in each direction with respect to the buoy were found. A new parameter, called significant displacement (Ds), is

introduced. It was calculated using a procedure identical to that of significant wave height (Hs), but this procedure was executed using the TriAXYS buoy displacement time series in each specific buoy reference frame DOF (instead of just using ocean surface displacements). The energy period (Te) was calculated following IEC TC-114 recommendations. Spectral moments (M_0 and M_{-1}) and energy periods (Te) were calculated as in [32], but as noted the Ds moments were calculated from the buoy frame displacements rather that the ocean surface elevation.

$$H_s = 4.004\sqrt{m_0} \qquad D_{s_{DOF}} = 4.004\sqrt{m_{0_{DOF}}} \qquad T_e = m_{-1}/m_0$$

Ds and Te were computed for each of the 5 DOFs of interest (surge, sway, heave, roll, and pitch), for each of the 7207 TriAXYS buoy datasets. These Ds-Te data points were grouped in bins similarly to the Hs-Te bins in the IEC approach mentioned above. Bin sizes for Hs based evaluation are standardized at values of 0.5m and 1s for Hs and Te, respectively. Bin sizes for Ds and Te were adjusted to give a reasonable resolution to the data sets selected for evaluation, and to account for the rotational units when considering the pitch and roll DOFs. For the rotational DOFs, the observed Te range was much more narrow banded than the energy periods observed for wave heights, and translational DOFs exhibited Ds ranges that were more concentrated than typical Hs distributions, thus those bin sizes were reduced to increase the resolution of the Ds-Te histograms. This resulted in 0.75 m Ds bin sizes for the X and Y directions, and 0.25 m Ds bin sizes for the Z direction. The Te bin sizes for the rotational data were reduced to 0.4 s. The charts in Figure 6.1 show the percentage of the 7207 TriAXYS datasets that fall within each Ds-Te bin for each DOF. The axis labels on the Te and Ds axes indicate the values at the bin centers.

Significant Displacement in the X-direction vs Energy Period

Ds [m] \ Te [seconds]	8.5	9.5	10.5	11.5	12.5	13.5	14.5	15.5	16.5	17.5
0.375	1	2	6	9	8	7	4	2	1	0
1.125	1	5	8	10	9	7	8	5	1	0
1.875	0	2	2	2	2	1	1	1	0	0
2.625	0	1	1	1	0	0	0	0	0	0

(a)

Significant Displacement in the Y-direction vs Energy Period

Ds [m] \ Te [seconds]	8.5	9.5	10.5	11.5	12.5	13.5	14.5	15.5	16.5	17.5
0.375	0	2	6	11	10	8	5	2	1	0
1.125	0	0	1	4	7	10	13	10	4	2
1.875	0	0	0	0	1	1	2	2	2	1
2.625	0	0	0	0	0	0	0	0	0	0

(b)

Significant Displacement in the Z-direction vs Energy Period

Ds [m] \ Te [seconds]	5.5	6.5	7.5	8.5
0.125	0	0	0	0
0.375	1	1	0	0
0.625	1	4	3	1
0.875	1	6	5	1
1.125	1	6	7	1
1.375	0	4	11	3
1.625	0	4	9	3
1.875	0	2	7	2
2.125	0	1	5	3
2.375	0	1	3	3
2.625	0	0	2	2
2.875	0	0	2	2
3.125	0	0	1	1

(c)

Significant Displacement in the Roll-direction vs Energy Period

Ds [°] \ Te [seconds]	1.5	1.7	1.9	2.1
1.1	0	0	0	0
3.4	0	0	0	0
5.7	0	0	0	0
8.0	1	1	0	0
10.3	2	3	0	0
12.6	2	6	3	0
14.9	1	8	7	2
17.2	0	8	9	3
19.5	0	7	6	5
21.8	0	5	6	5
24.1	0	1	5	3
26.4	0	0	2	1

(d)

Significant Displacement in the Pitch-direction vs Energy Period

Ds [°] \ Te [seconds]	1.5	1.7	1.9	2.1
1.1	0	0	0	0
3.4	0	0	0	0
5.7	0	0	0	0
8.0	1	1	0	0
10.3	2	3	1	0
12.6	2	6	4	0
14.9	1	7	7	1
17.2	1	7	8	2
19.5	0	7	8	2
21.8	0	4	9	3
24.1	0	1	8	3
26.4	0	0	3	2

(e)

Figure 6.1 – Significant displacement histogram results for each degree of freedom (a) Surge (b) Sway (c) Heave (d) Roll (e) Pitch

It is interesting to compare the Z direction significant displacement with the significant wave height since one may reasonably expect them to be similar, but as the buoy rides over the waves, it changes orientation and so the translational motion in the local frame Z direction doesn't match the vertical motion profile of the wave. As the WECO is installed and oriented with the local frame, it is important to consider these local frame displacements when assessing which WECO configuration has the maximum opportunity for power production. Figure 6.2 shows the Hs-Te chart, along with the Z-direction Ds-Te chart; for this specific comparison, the Ds-Te bin structures have been adjusted to match the Hs-Te standard. For the same wave data, the Z-direction motion is more tightly grouped with over 50% of all datasets falling into just 4 bins. For the dataset selections, the Z-direction displacement bin size was decreased until the maximum percentage of datasets falling in a single bin was 11%, see Figure 6.1(c). This indicated that the results from applying datasets selected for oscillations in different DOFs would likely yield different average power estimates.

Significant Wave Height vs Energy Period

Hs [m] \ Te [seconds]	5.5	6.5	7.5	8.5	9.5
0.25	0	0	0	0	0
0.75	1	3	3	1	0
1.25	2	6	6	4	1
1.75	1	4	8	5	1
2.25	0	4	8	8	2
2.75	0	2	5	6	2
3.25	0	1	3	4	2
3.75	0	0	2	2	2
4.25	0	0	1	2	2

(a)

Significant Displacement in the Z-direction vs Energy Period

Ds [m] \ Te [seconds]	5.5	6.5	7.5	8.5	9.5
0.25	1	1	0	0	0
0.75	2	11	8	1	0
1.25	2	10	18	4	0
1.75	0	6	16	5	1
2.25	0	2	8	5	0
2.75	0	0	4	3	1
3.25	0	0	1	1	1
3.75	0	0	0	0	0
4.25	0	0	0	0	0

(b)

Figure 6.2 – Significant wave height and Z-dir significant displacement histogram results (a) Hs (b) Ds-Z

Each dataset that had the Ds-Te value closest to the center of each bin was selected to represent that bin, as is done in the IEC TC 114 approach. Any bin with less than 70 of the 7207 datasets (~1%) was considered insignificant and excluded from further analysis. This lead to a list of representative datasets to be applied for each direction of motion, ranging from 18 to 27 individual datasets depending on the DOF. The average power results from each dataset were

weighted against the others based on the proportion of datasets they represent, i.e. how many datasets fell within that displacement/period bin.

Each WECO configuration was reviewed to discover which directions of buoy motion were likely to excite it the most. Table 6.1 lists which DOF Ds-Te selected datasets were selected for each WECO configuration. The IEC TC-114 selected Hs-Te datasets were used with all WECOs so that the results from the new Ds-Te approach can be compared to the accepted Hs-Te approach.

Table 6.1 – Selected dataset groups to apply to each WECO design and location

Topology	Location1	Location2
Rotating Short	Z, Roll, Pitch, Hs	Z, Roll, Pitch, Hs
Rotating Long	Z, Roll, Pitch, Hs	Z, Roll, Pitch, Hs
Linear X	X, Pitch, Hs	X, Pitch, Hs
Linear Y	Y, Roll, Hs	Y, Roll, Hs
Linear Z	Z, Roll, Hs	Z, Pitch, Hs

With the representative datasets selected, a theoretical ceiling of average winter power generation was evaluated for each of the 10 WECO configurations, while satisfying the maximum oscillation amplitude restriction, evaluated in Section 2.2. To reach this goal, spring rates were tuned so that the undamped natural frequency of the WECO matched the energy period of the bin center $\left(1/T_e = \sqrt{k_{spring}/m_{WECO}}\right)$ that the applied dataset was selected to represent, and the damping ratio was adjusted through iterative loops so that the maximum WECO oscillation was within 7% of the allowable maximum for that WECO. It is possible that alternative spring stiffness values may have produced more power than the one selected, but since this analysis was strictly comparative this ensured an equal analysis for each WECO without the additional computation time required to optimize the spring rate along with the damping ratio.

The average power generated for each 20 minute period was calculated from the simulated motion of the WECO using (16). These individual values were weighted and averaged based on the percentage of occurrences of that wave condition, as per the IEC TC-114 approach (i.e. how many datasets fell within that displacement/period bin), to estimate the theoretical ceiling of average WECO power that could be generated throughout the winter months for each WECO configuration.

Table 6.2 lists the results of the comparative analysis. These theoretical ceilings of average winter power output are for comparison only as they use the tuned spring rate and damping ratios

described earlier in this section. Powers are listed for each selection of datasets listed in Table 6.1. The highest theoretical ceiling of average winter power output for this analysis was 1.53 W for a linear X direction WECO installed in location 1, and occurred when subjected to the load datasets selected based on the standard IEC TC-114 Hs-Te approach. This result was followed closely by the linear Z direction WECO installed in location 2, at 1.42 W, and that theoretical ceiling of average winter power occurred when using the load datasets selected for their Z direction Ds values.

It is interesting that for the linear X direction WECO, the datasets selected based on their Ds in the X direction resulted in a lower average power than the Hs selections. The reason for this is unknown, and the difference in the estimated average powers is small enough that it could be simply due to chance in what other wave events were included in the datasets that were selected based on the wave event that was the peak for that frequency. There is also a possibility that some selected datasets have two peaks in their Hs-Te or Ds-Te plots that could produce a Te value that does not actually match with either of the peaks, as noted in [33]. This could introduce further errors in the estimation of average power, but these are expected to have similar effects across all devices. The results for the linear Z direction WECO followed expectations with higher estimated powers resulting from datasets selected based on their motion in the same DOF as the WECO motion.

Table 6.2 - Results of comparative analysis, average estimated power output through the winter months from November to March

	Ds direction used for TriAXYS dataset selection					
WECO Configuration	Surge (X)	Sway (Y)	Heave (Z)	Roll (about X)	Pitch (about Y)	Significant Wave Height (H_s) TC-114
L1Sht			0.56	0.51		0.53
L2Sht			0.54	0.48	0.47	0.52
L1Lng			0.47	0.42	0.42	0.45
L2Lng			0.37	0.42	0.30	0.35
L1X	1.39				1.14	1.53
L2X	1.36				1.10	1.48
L1Y		0.83		0.65		0.85
L2Y		0.84		0.67		0.87
L1Z			1.40	1.23		1.35
L2Z			1.42		1.17	1.36

The highest estimated theoretical ceiling of power with a variable spring rate and damping ratio were generated by the linear X and linear Z WECOs. The difference in power between installation in location 1 or 2 was negligible. The linear X direction WECO installed in location 1 (L1X), and the linear Z direction WECO installed in location 2 (L2Z) were selected to find static spring rate and damping ratio pair, as that is what is envisioned for the actual constructed devices rather than the variable spring rates and damping ratios that were used for comparative analysis, that would generate the highest average power generation through the winter months.

6.2 Average Winter Power Analysis of Selected WECO Configurations

For the comparative analysis in Section 6.1, the spring rate was adjusted so that the undamped natural frequency of the WECO was equal to the oscillating frequency that the applied dataset had been selected for in the Hs or Ds vs Te charts. This was necessary to provide a fair comparative analysis, but it is unrealistic to expect the WECO to tune its spring rate and damping to the frequency of the waves being applied while maintaining a simple design. This section explains how static spring rate and damping pairs were found that limit the single peak oscillation amplitude of the selected configurations, L1X and L2Z, to their maximum allowable amplitudes, evaluated in Section 2.2, across the spectrum of wave events throughout the winter. These static values are used to evaluate a realistic estimate of the average winter power that would be generated by the selected configurations if constructed in the envisioned manner.

For each of the two selected configurations, L1X and L2Z, a range of static spring rates was established based on those that had been selected for the comparative analysis. With the goal of determining the ζ value for each spring rate that would maximize the WECO stroke in a single peak excitation event, while maintaining all other oscillations under that value, a selection of datasets was sought that was most likely to cause the peak oscillation amplitudes for each WECO configuration. To this end, the recorded buoy motions were evaluated to find the datasets that contained the peak oscillation amplitudes in each DOF and frequency bin. Frequency bin sizes were selected based on the 1s period spacing recommended by IEC TC-114 for periods between 6s and 30s, but under 6 seconds a frequency spacing of .1 Hz was selected so that a higher resolution of frequencies could be investigated, resulting in 33 frequency bins. Datasets were selected that either contained the single largest peak amplitude within each frequency band, or that contained the largest average amplitude over each frequency band, resulting in between 58 and 94 datasets depending on the WECO configuration.

A range of spring rates was tested for all of the maximum oscillation amplitude datasets, for the selected configurations L1X and L2Z, and the associated minimum damping ratio required to satisfy the maximum allowable oscillation amplitude constraint was discovered. Models of the selected configurations were set up for each spring rate, and the buoy and WECO motions were simulated for each of the maximum amplitude datasets described above. For each configuration

and spring rate combination, the damping ratio was adjusted through an iterative loop for each dataset until the maximum oscillation amplitude was within 1% of the maximum allowable.

For each configuration and spring rate, there was one dataset that required the maximum ζ value to limit the oscillation amplitude to the maximum allowable, these pairs of spring rate and damping ratios were recorded. Due to the dataset selection process above, each of these spring rate and damping ratio pairs would set the single maximum WECO oscillation amplitude, during the most severe wave event for the specific WECO configuration that occurred through the sampling period of two winters, to the maximum allowable amplitude. It is therefore likely that minimal damage would occur to the WECO if any of these spring rate and damping pairs were selected and a slightly more severe wave event occurred.

As a damping ratio was found for each WECO configuration and spring rate, the average winter power potential was computed based on the IEC TC-114 approach rather than the Ds-Te approach, so that the results would be from the same datasets and could be compared directly. Also, there was little variation between the power estimates from the Hs-Te approach and the Ds-Te approach. To avoid running unnecessary simulations, a staggered selection of spring rate and damping ratio pairs was run first and the average winter power was calculated and plotted. It was apparent from early results that there would be a single peak to the power outputs, and some spring/damping pairs were not simulated when it was known they would not provide the maximum average power because of the low results of nearby pairs.

Table 6.3 and Figure 6.3 show the results from the models with the highest power producing spring rate and damping pairs selected for the L1X WECO to meet the maximum oscillation amplitude requirements for all of the recorded datasets, along with the estimated average winter power generated based on the IEC TC-114 approach (Hs-Te selected datasets). Table 6.4 and Figure 6.4 show the corresponding information for the L2Z WECO.

Table 6.3 – Spring rate and damping ratio pairs with associated average winter power estimates for the linear X WECO installed in location 1

L1X WECO Configuration		
Spring Rate (k) [N/m]	Damping Ratio (ζ)	Average Winter Power [W]
100	11.18	0.302
200	7.71	0.302
700	2.12	0.427
800	1.66	0.445
925	1.35	0.434
1050	1.13	0.410

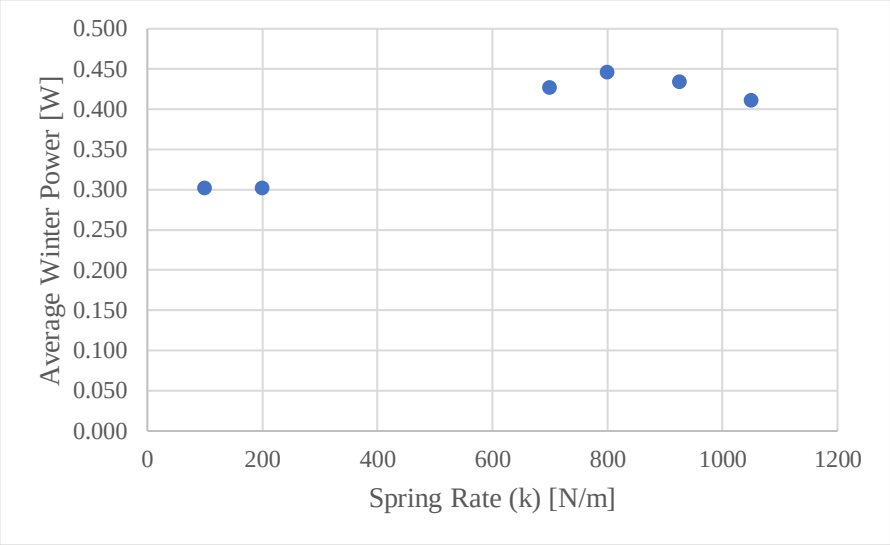

Figure 6.3 – Average winter power compared to spring rate for the linear X WECO installed in location 1

Table 6.4 – Spring rate and damping ratio pairs with associated average winter power estimates for the linear Z WECO installed in location 2

L2Z WECO Configuration		
Spring Rate (k) [N/m]	Damping Ratio (ζ)	Average Winter Power [Watts]
50	27.85	0.445
300	10.90	0.448
700	6.09	0.480
925	4.92	0.484
1200	3.77	0.496
1400	2.96	0.515
1600	2.13	0.537
1700	1.80	0.536
1800	1.40	0.530
2000	0.61	0.409

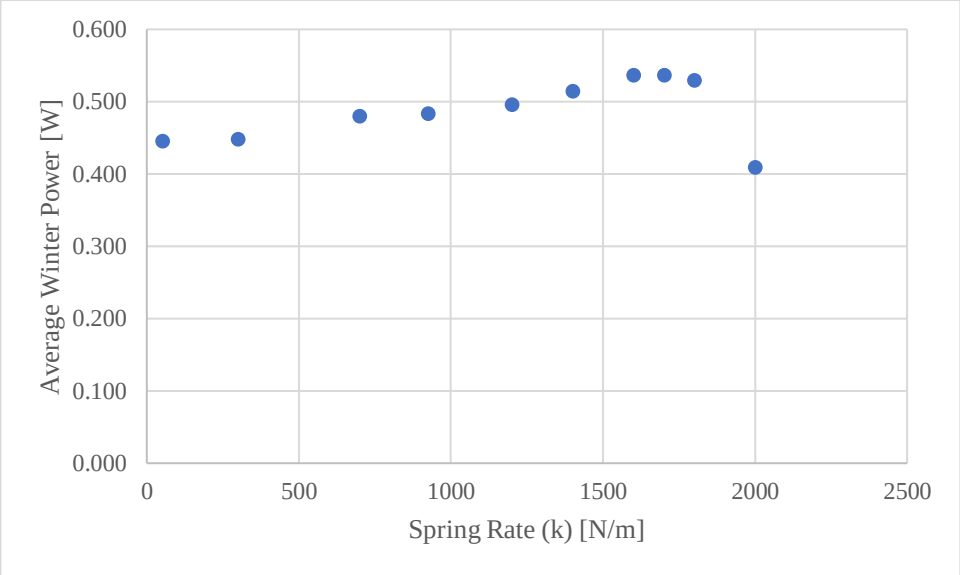

Figure 6.4 - Average winter power compared to spring rate for the linear Z WECO installed in location 2

The above tables and figures, shows that most of the damping ratios were above 1 (overdamped). Damping ratios in the underdamped range (<1) were considered, but in order to

satisfy the maximum oscillation amplitude restriction the spring rates were very high and resulted in extremely low power generation.

The maximum average winter power potential was produced by the linear Z WECO installed in location 2. The maximum estimated power output is 0.537 W and was associated with a spring rate of 1600 N/m and a damping ratio of 2.13. A spring rate of 1700 N/m and a damping ratio of 1.8 produced a very similar estimate for average winter power generation. A close second for maximum average winter power potential was the linear X WECO installed in location 1. With a spring rate of 800 N/m and a damping ratio of 1.66, the estimated power output is 0.445 W.

6.3 Effect of WECO on Buoy Motion

The most important constraint on the WECO was that it could not significantly affect buoy motion as this would corrupt the inputs to the wave measurement algorithm. A significant change to buoy motion with a WECO installed would also call into question the accuracy of the results of this thesis, because the state dependant loads on the buoy would not be valid if the simulated buoy followed a different trajectory from the original.

Figure 6.5 shows the FFT of the original buoy motion, the motion of the buoy with the L1X WECO installed, and the motion of the buoy with the L2Z WECO installed. The simulated original buoy displacement is also included in Figure 6.5 since this is expected to be more similar to the displacements with the WECO's installed, and would highlight the effects of allowing the WECO to move. These plots were created in the same manner as those in Figure 5.1, so any discrepancy would be accentuated due to summing the results from the application of different load datasets. The FFT plots for each DOF are very similar, and the time series plots in Figure 6.6 are close. The effects on buoy motion with the two selected configurations are acceptable and should not significantly affect buoy motion and/or the wave data derived from these motions.

Table 6.5 and Table 6.6 list the Pearson correlation coefficients (r values) for the original buoy motion and buoy motion with the L1X and L2Z WECOs installed, respectively. The minimum r values were 0.95 and 0.99 for the L1X and L2Z WECOs, respectively. These r values indicate a very close correlation of the buoy displacement time series data for both WECOs.

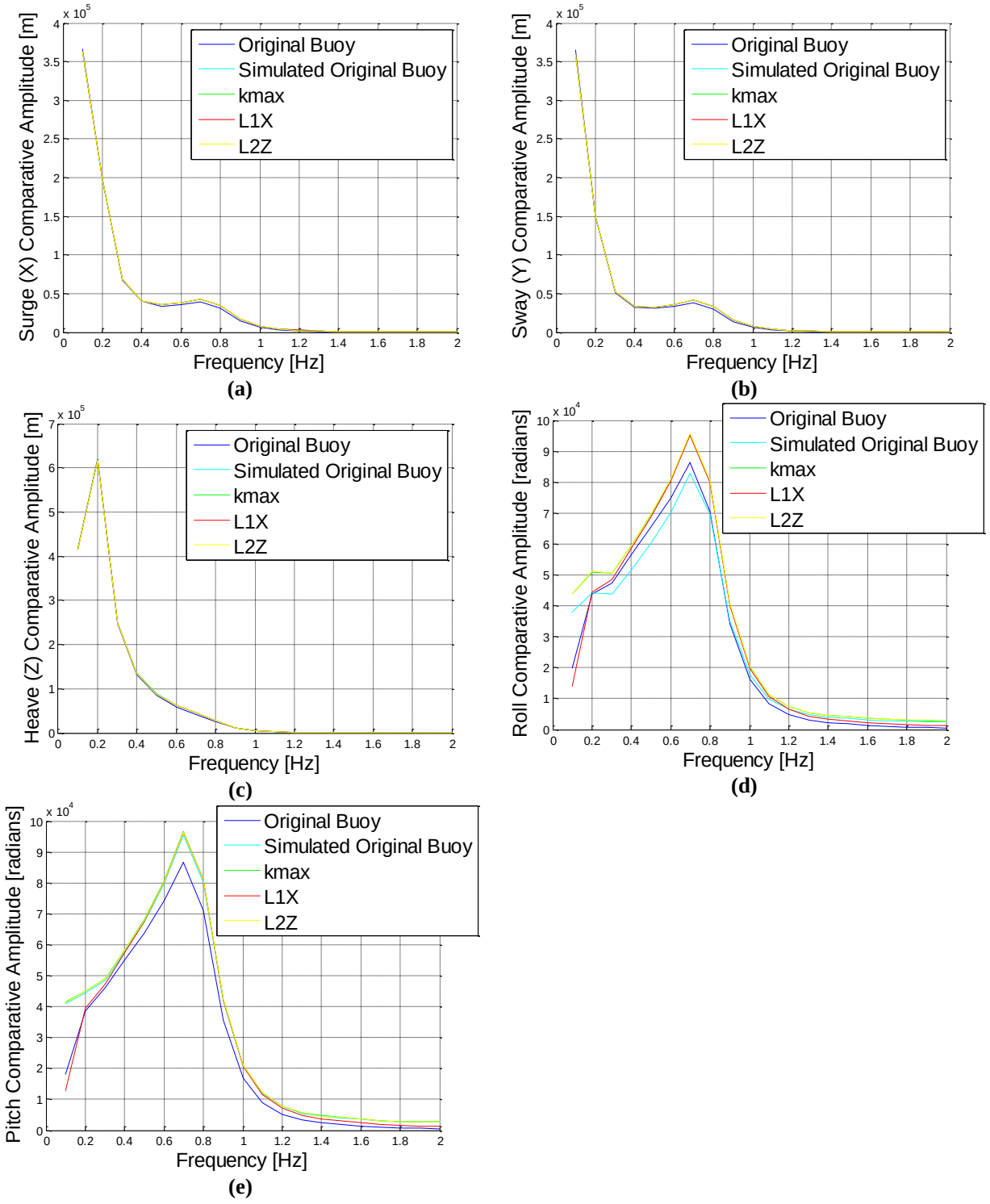

Figure 6.5 – Comparison of the motion of the original buoy, simulated original buoy, linear X WECO installed in location 1 (L1X), and linear Z WECO installed in location 2 (L2Z) in (a) Surge (b) Sway (c) Heave (d) Roll (e) Pitch

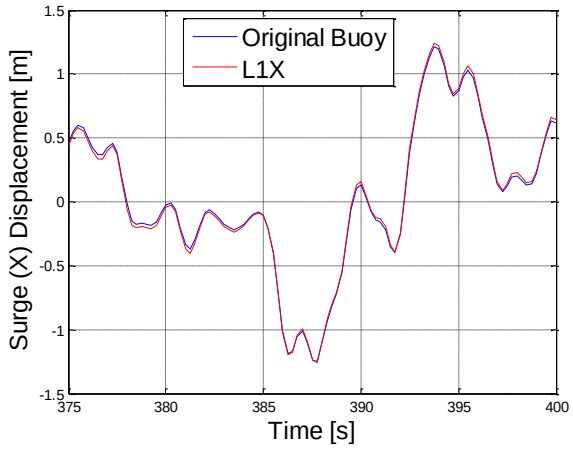
Original Buoy
L1X
Surge (X) Displacement [m]
Time [s]

(a)

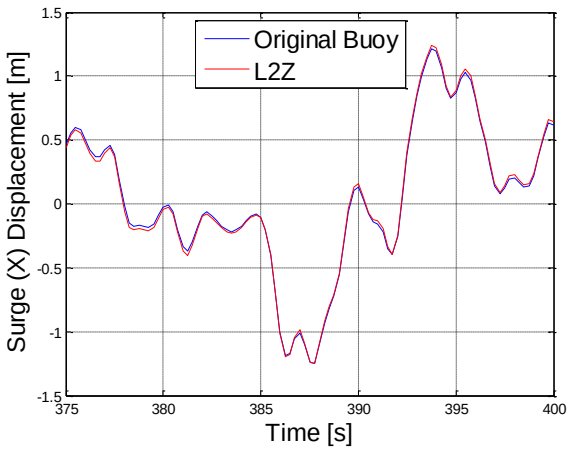
Original Buoy
L2Z
Surge (X) Displacement [m]
Time [s]

(f)

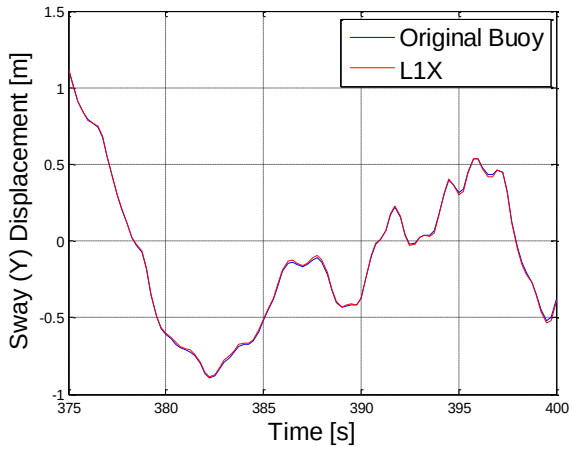
Original Buoy
L1X
Sway (Y) Displacement [m]
Time [s]

(b)

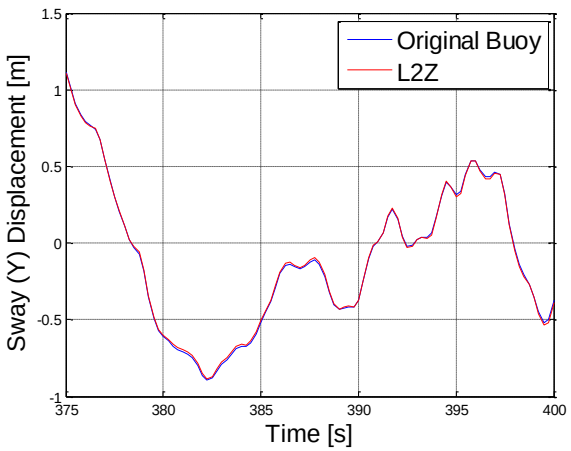
Original Buoy
L2Z
Sway (Y) Displacement [m]
Time [s]

(g)

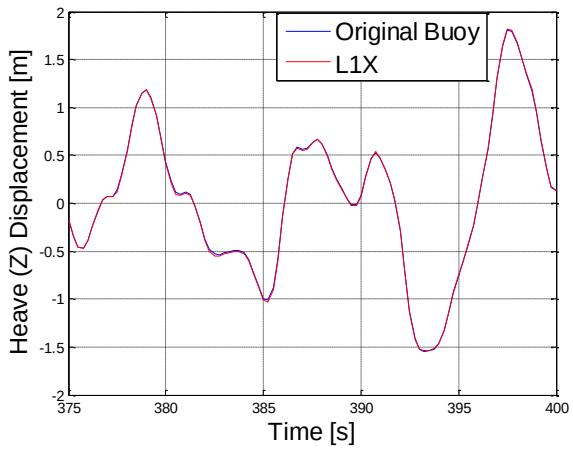
Original Buoy
L1X
Heave (Z) Displacement [m]
Time [s]

(c)

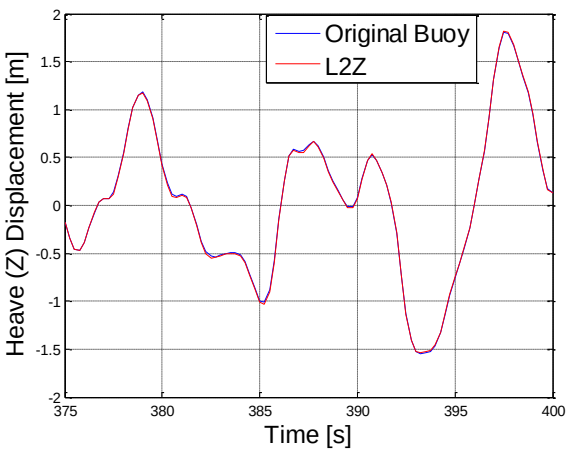
Original Buoy
L2Z
Heave (Z) Displacement [m]
Time [s]

(h)

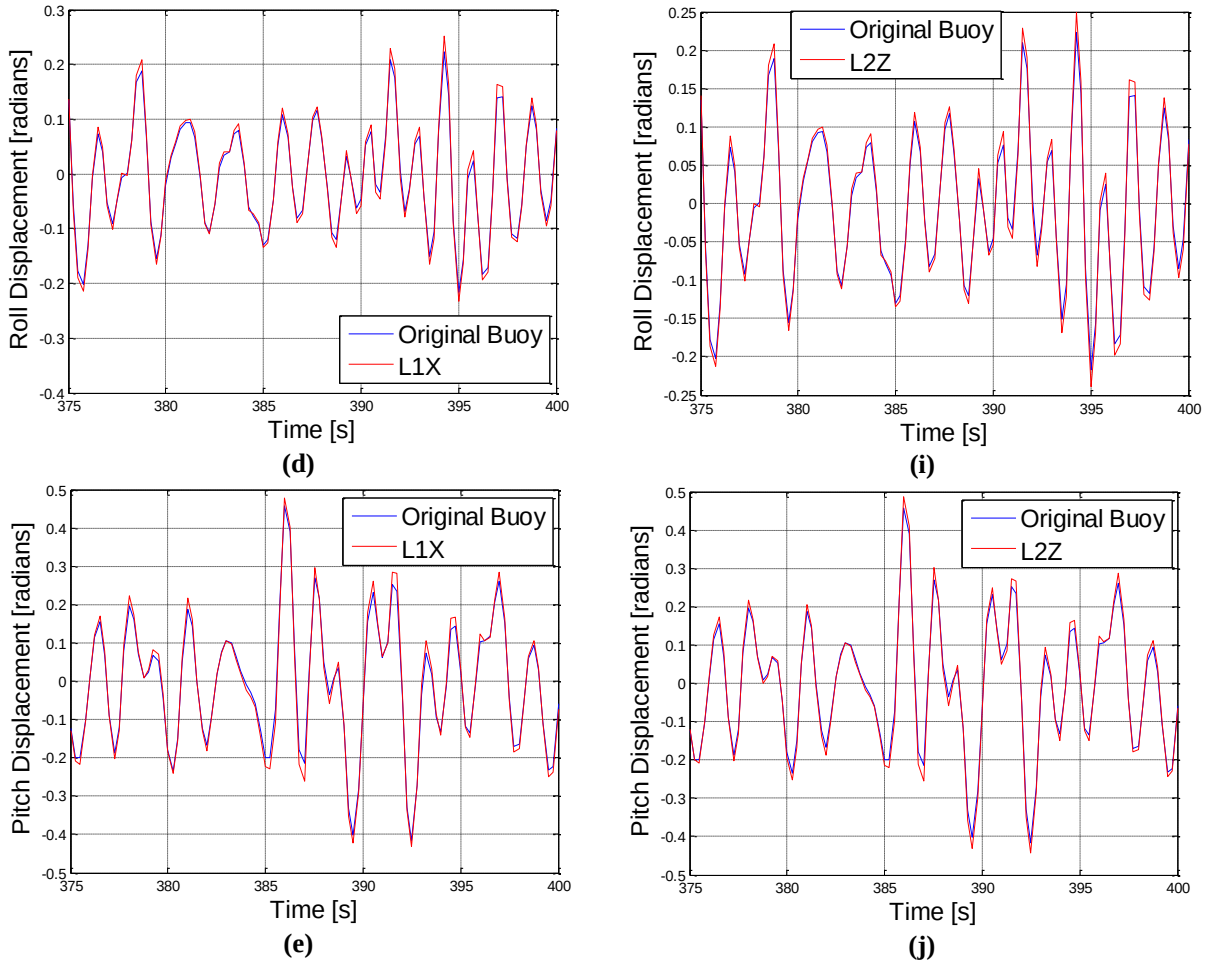

Figure 6.6 - Comparison time series plots of the original buoy motion, with L1X in the left column (a thru e) and L2Z in the right column (f thru j)

Table 6.5 - Pearson correlation coefficients for the original and L1X buoy motion

Dataset	1	2	3	4	5	6	7	8	9	10	11	12	13	14
Suge	1.00	1.00	1.00	0.99	1.00	1.00	1.00	1.00	1.00	1.00	1.00	1.00	1.00	1.00
Sway	1.00	1.00	0.99	1.00	1.00	1.00	1.00	0.99	1.00	1.00	1.00	1.00	1.00	1.00
Heave	1.00	1.00	1.00	1.00	1.00	1.00	1.00	1.00	1.00	1.00	1.00	1.00	1.00	1.00
Roll	1.00	0.98	1.00	1.00	1.00	0.95	0.99	1.00	0.99	1.00	0.99	1.00	1.00	0.99
Pitch	0.99	1.00	1.00	0.99	0.99	0.95	1.00	1.00	1.00	0.98	1.00	1.00	1.00	0.99
Dataset	**15**	**16**	**17**	**18**	**19**	**20**	**21**	**22**	**23**	**24**	**25**	**26**	**27**	
Suge	1.00	1.00	1.00	1.00	1.00	1.00	1.00	1.00	1.00	1.00	1.00	1.00	1.00	
Sway	1.00	1.00	1.00	1.00	0.99	1.00	1.00	1.00	1.00	0.99	1.00	1.00	1.00	
Heave	1.00	1.00	1.00	1.00	1.00	1.00	1.00	1.00	1.00	1.00	1.00	1.00	1.00	
Roll	1.00	1.00	1.00	0.96	1.00	1.00	1.00	0.98	0.97	0.99	0.99	1.00	1.00	
Pitch	1.00	1.00	1.00	1.00	1.00	0.98	1.00	1.00	1.00	0.99	1.00	1.00	0.99	

Table 6.6 - Pearson correlation coefficients for the original and L2Z buoy motion

Dataset	1	2	3	4	5	6	7	8	9	10	11	12	13	14
Suge	1.00	1.00	1.00	0.99	1.00	1.00	1.00	1.00	1.00	1.00	1.00	1.00	1.00	1.00
Sway	1.00	1.00	0.99	1.00	1.00	1.00	1.00	0.99	1.00	1.00	1.00	1.00	1.00	1.00
Heave	1.00	1.00	1.00	1.00	1.00	1.00	1.00	1.00	1.00	1.00	1.00	1.00	1.00	1.00
Roll	1.00	1.00	1.00	1.00	1.00	1.00	1.00	1.00	1.00	1.00	1.00	1.00	1.00	0.99
Pitch	1.00	1.00	1.00	1.00	1.00	1.00	1.00	1.00	1.00	1.00	1.00	0.99	1.00	0.99
Dataset	15	16	17	18	19	20	21	22	23	24	25	26	27	
Suge	1.00	1.00	1.00	1.00	1.00	1.00	1.00	1.00	1.00	1.00	1.00	1.00	1.00	
Sway	1.00	1.00	1.00	1.00	0.99	1.00	1.00	1.00	1.00	0.99	1.00	1.00	1.00	
Heave	1.00	1.00	1.00	1.00	1.00	1.00	1.00	1.00	1.00	1.00	1.00	1.00	1.00	
Roll	1.00	1.00	1.00	0.99	0.99	0.99	0.99	0.99	0.99	0.99	0.99	0.99	0.99	
Pitch	1.00	1.00	1.00	1.00	0.99	1.00	0.99	1.00	1.00	0.99	1.00	0.99	0.99	

Figure 6.7 shows the summed amplitudes of the FFTs of the oscillating WECO masses for the L1X and L2Z configurations. The L2Z configuration has a peak power frequency of approximately 0.2Hz, and most power is harvested within the range of wave measurement frequencies, 0.03 to 0.63 Hz. Most of the power generated by the L1X configuration is harvested above the maximum wave frequency threshold of measurement of 0.63 Hz. This indicates that although the L1X configuration may generate less power than the L2Z configuration, it is likely to have less impact on wave measurements. However, it should be noted that the amplitudes of simulated buoy motions were larger than the original buoy in and around the WECO mass peak frequency of 0.7 Hz, see Figure 5.1(a) and Figure 6.5(a), which indicate that the power estimate for the L1X WECO may be inflated.

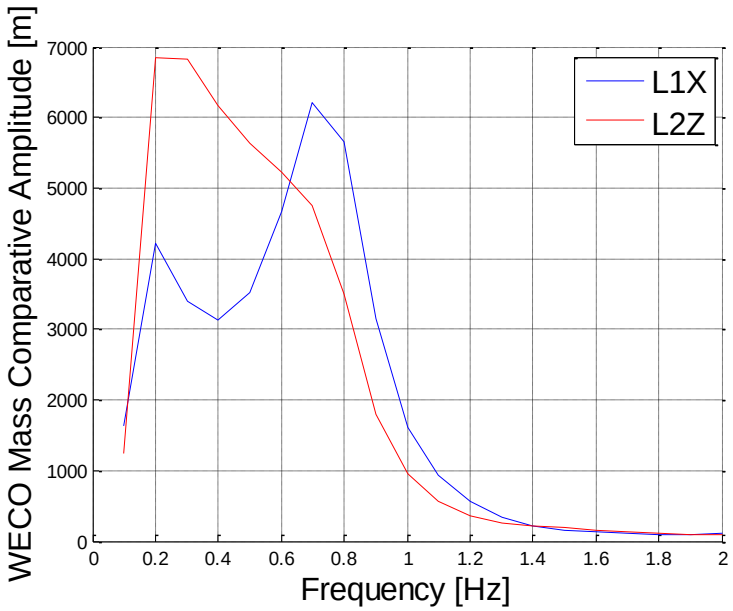

Figure 6.7 - Comparison of the WECO mass oscillating motion for the L1X and L2Z designs

Chapter 7
Conclusions

The primary goal of this research was to find the WECO device or devices that would generate the most power without affecting buoy motion and / or wave data produced from that motion. A second goal was to utilize the recorded motions of a TriAXYS buoy installation to evaluate the loads applied to that buoy and use them for simulating models of TriAXYS buoys with different WECO configurations installed. Environmental loads that were applied to a TriAXYS buoy stationed off the coast of Ucluelet, BC were derived from the recorded motion and mass properties of the buoy, extracted from a 3D CAD model. These loads included wind, waves, and mooring, and the data spanned the winter months of November to March, 2014 to 2016.

Five WECO designs were developed, each of which focused on a different DOF of buoy motion for power capture (surge, sway, heave, roll, and pitch). Two unique battery locations in the TriAXYS buoy were identified, and two others were mirrored from these and would be subjected to very similar motions. Dynamic models of the 10 TriAXYS buoy-WECO configurations, five designs in two locations, were derived using the Lagrange method utilizing Rayleigh's dissipation function to represent the PTO. Subsets of force and moment time histories were selected based on the IEC TC-114 recommendations, to find a representative selection of data for motion in each specific DOF rather than for significant wave height. This resulted in five subsets of data, each selected for their motion in either the surge, sway, heave, roll, or pitch directions. A new parameter to categorize wave states was introduced, significant displacement (Ds). It is similar to Hs but is derived from the displacements of the buoy in its local frame of reference, rather than ocean surface displacements. The WECO configurations were analyzed to find the DOFs of buoy motion that were most likely to excite them, and the subsets of loads selected for their displacements in those DOFs were applied to those WECOs.

Forward integrated time based simulations were conducted for all configurations, applying the appropriate subset of loads selected for each configuration. Buoy motion from the simulations was compared to the original buoy data, and the difference between the simulated motions and the original buoy motion was determined to be acceptable. All of the time series plots showed that the simulated buoy motion following the original motion very closely. Thus, all of the configurations were deemed feasible with regards to the constraint of not affecting buoy motion.

The two most promising configurations both had high power outputs and did not affect buoy motion. They are the linear WECO that moved in the surge (X) direction (see Figure 2.6) and was installed in location 1 (L1X) (see Figure 2.2), and the linear WECO that moved in the heave (Z) direction (see Figure 2.8) and was installed in location 2 (L2Z) (see Figure 2.2). These were simulated for a subset of load datasets selected using the standard IEC TC-114 approach, so the results could be compared. Static spring rate and damping ratio pairs were determined to find the tuning that would generate the highest average power, while limiting the maximum oscillation amplitude of the device when subjected to peak wave events to within the battery envelope. The estimated average winter power and associated spring rate and damping ratio for each of the selected WECO configurations are shown in Table 7.1. The Pearson r values when comparing buoy motion between the original buoy and the L1X and L2Z designs were 0.95 and above for all DOFs and datasets.

Table 7.1 - Estimated average winter power generation for the two selected WECO configurations

WECO Configuration	Power (Watts)	Spring Rate (N/m)	Damping Ratio
L1X	0.445	800	1.66
L2Z	0.537	1600	2.13

While these results are lower than the required power of 0.75W, there is still an opportunity to increase the power generated using more advance controls such as latching or variable spring rate and/or damping coefficients. Variable spring rate and damping ratios were shown to produce a theoretical power output ceiling of L1X and L2Z of 1.53W and 1.42W, respectively. It is possible that a device could be designed to adapt to varying wave excitations and have a high enough energy conversion efficiency to output the required 0.75W of electrical power. Detailed mechanical design and testing of the selected configurations may lead to an increase in the energy captured. One such option could be soft end stops for the WECO mass, to protect against mechanical failure and data degradation, that could increase overall WECO motion and average power potential, while using simple static spring rates and/or damping ratios. The approach of evaluating load data from buoy motion is considered successful, and could be adopted for other buoys and / or deployment sites where motions are known, to evaluate what WECO configuration is best suited and if a viable device exists.

Chapter 8 Bibliography

[1] AXYS Technologies, "TRIAXYS ™ Directional Wave Buoy," *Product Brochure*. 2011.

[2] M. E. McCormick, "A modified linear analysis of a wave-energy conversion buoy," *Ocean Eng.*, vol. 3, no. 3, pp. 133–144, 1976.

[3] M. S. Lagoun, A. Benalia, and M. E. H. Benbouzid, "Ocean wave converters :state of the art and current status," *Converter*, pp. 636–641, 2010.

[4] R. QUINNELL, "Energy scavenging offers endless power," *Electronic Design*, 2009.

[5] J.-C. Gilloteaux, "Etude bibliographique sur le déferlement des vagues et extension au Cas tridimensionnel du système SEAREV," Ecole Centrale de Nantes, 2003.

[6] A. Babarit and M. Guglielmi, "Device for converting wave energy into useable energy, particularly electrical energy, and associated method," US 201110089690 Al, 2009.

[7] A. Clement, A. Babarit, and G. Duclos, "Apparatus for converting wave energy into electric power," vol. 111111, no. 19, 2009.

[8] A. Babarit and A. H. Clément, "Shape optimisation of the SEAREV wave energy converter," in *World Renewable Energy Congress*, 2006.

[9] A. Babarit and A. Clement, "Optimal latching control of a wave energy device in regular and irregular waves," *Appl. Ocean Res.*, vol. 28, no. 2, pp. 77–91, 2006.

[10] A. Babarit, M. Guglielmi, and A. H. Clément, "Declutching control of a wave energy converter," *Ocean Eng.*, vol. 36, no. 12–13, pp. 1015–1024, 2009.

[11] C. Josset, A. Babarit, and a H. Clément, "A wave-to-wire model of the SEAREV wave energy converter," *Proc. Inst. Mech. Eng. Part M J. Eng. Marit. Environ.*, vol. 221, no. 2, pp. 81–93, Jan. 2007.

[12] J. Cordonnier, F. Gorintin, A. De Cagny, A. H. Clément, and A. Babarit, "SEAREV: Case study of the development of a wave energy converter," *Renew. Energy*, vol. 80, pp. 40–52, Aug. 2015.

[13] "Projet prometteur : le Searev – energies2demain.com." [Online]. Available: http://energies2demain.com/eau/vagues/projet-prometteur-le-searev.

[14] a Mccabe, a Bradshaw, J. Meadowcroft, and G. Aggidis, “Developments in the design of the PS Frog Mk 5 wave energy converter,” *Renew. Energy*, vol. 31, no. 2, pp. 141–151, Feb. 2006.

[15] R. E. Gemmell and A. Muetze, “Discussion of a new rocking buoy reaction based wave energy converter topology,” in *International Conference on Electrical Machines*, 2010.

[16] Y. Zhang, C. Wu, and Z. Dong, “A new wave energy conversion method based on inertial pendulum,” vol. 3, no. 2, pp. 222–230, 2007.

[17] Y. Zhang and Z. Dong, “Modeling of wave energy absorption based on BP neural network for underwater vehicles,” in *World Congress on Intelligent Control and Automation*, 2008, pp. 2225–2229.

[18] C.-A. Reymondin, *The theory of horology*. The technical college of the Vallee de Joux, 1999.

[19] M. Cheong Lei, L. Xie, and R. Du, “Kinematic analysis of an auto-winding system with the pawl-lever mechanism and its application in energy harvesting,” *Int. J. Mech. Sci.*, vol. 52, no. 12, pp. 1605–1612, Dec. 2010.

[20] L. Xie, C. G. Menet, H. Ching, and R. Du, “The automatic winding device of a mechanical watch movement and its application in energy harvesting,” *J. Mech. Des.*, vol. 131, no. 7, p. 71005, 2009.

[21] T. Hara, J. Kitahara, Y. Oshima, and H. Makiba, “Analog indicator type electronic timepiece and charging method thereof,” 5581519, 1996.

[22] R. E. Salomon, “Process and apparatus for converting rocking motion into electrical energy,” 4719158, 1988.

[23] A. Goldin, “Gyroscope-based electricity generator,” 7375436, 2008.

[24] N. J. Baker, “Linear generators for direct drive marine renewable energy converters,” University of Durham, 2003.

[25] J. K. H. Shek, D. E. Macpherson, and M. a. Mueller, “Experimental verification of linear generator control for direct drive wave energy conversion,” *IET Renew. Power Gener.*, vol. 4, no. 5, p. 395, 2010.

[26] P. R. . Brooking and M. A. Mueller, “Power conditioning of the output from a linear vernier hybrid permanent magnet generator for use in direct drive wave energy converters,” *IEE Proceedings-Generation, Transm. Distrib.*, 2005.

[27] M. a. Mueller, “Electrical generators for direct drive wave energy converters,” *IEE Proc. - Gener. Transm. Distrib.*, vol. 149, no. 4, p. 446, 2002.

[28] A. Babarit, A. Clément, J. Ruer, and C. Tartivel, “SEAREV: a fully-integrated wave energy converter,” 2006.

[29] R. Mahanty and P. Gupta, “Application of RBF neural network to fault classification and location in transmission lines,” *IEE Proceedings-Generation, Transm. …*, vol. 151, no. 3, pp. 201–212, 2004.

[30] M. D. Miles, E. Mansard, T. Vandall, and R. Phillips, “TRIAXYS directional wave buoy,” in *Canadian Coastal Conference*, 2003.

[31] IEC, “IEC TS 62600-101 Marine energy - Wave, tidal and other water current converters - Part 101: Wave energy resource assessment and characterization,” 2015.

[32] M. Folley, *Numerical modelling of wave energy converters: state-of-the-art techniques for single wec and converter arrays*. 2016.

[33] B. Robertson, H. Bailey, D. Clancy, J. Ortiz, and B. Buckham, “Influence of wave resource assessment methodology on wave energy production estimates,” *Renew. Energy*, vol. 86, pp. 1145–1160, 2016.